UNIVERSITÉ DU QUÉBEC À MONTRÉAL

UTILISATION DU CONTENU EN INFORMATION POUR OPTIMISER LES CANAUX D'INSTRUMENTS SATELLITAIRES DANS L'INFRAROUGE THERMIQUE ET LOINTAIN

THÈSE

PRÉSENTÉE

COMME EXIGENCE PARTIELLE

DU DOCTORAT EN SCIENCES DE LA TERRE ET DE L'ATMOSPHÈRE

PAR

LAURENCE COURSOL

OCTOBRE 2023

CHAPITRE I

REMERCIEMENTS

Je tiens à remercier mon directeur de recherche, le Professeur Pierre Gauthier, pour sa disponibilité et son soutien tout au long de mon doctorat. Sans lui, je n'aurais pu en apprendre autant sur l'assimilation de données grâce à nos nombreuses discussions. Je remercie également des collaborateurs qui ont été essentiels à cette thèse, soit le Professeur Jean-Pierre Blanchet, le Dr. Quentin Libois et le Dr. Sylvain Heilliette. Ces personnes ont répondu à mes nombreuses questions qui m'ont permis d'en apprendre énormément sur la télédétection et l'assimilation de données.

Sur une note plus personnelle, je tiens aussi à remercier mes collègues de bureau qui sont venus et repartis au gré de leurs études. De plus, merci à mes ami.e.s Valérie, Gabrielle, Lydia, JS, Émilie, Yann et Simon pour m'avoir soutenue, écoutée quand je râlais et botter les fesses aux moments nécessaires. Merci Mathieu d'être là et pour ta patience, jongler une thèse et une relation est un petit exploit. Merci aussi à ma famille et ma mère Sylvie pour leur support, sans qu'iels comprennent exactement mon travail, et plus particulièrement mon père, Michel, qui m'a fourni les outils nécessaires.

TABLE DES MATIÈRES

LISTE DES TABLEAUX

LISTE DES FIGURES

LISTE DES ABRÉVIATIONS

AIRS	Atmospheric Infrared Sounder
AMSU	Advanced Microwave Sounding Unit
CLARREO	Climate Absolute Radiance and Refractivity Observatory
CNRM	Centre National de Recherches Météorologiques
CrIS	Cross-track Infrared Sounder
DFS	Degrees of Freedom per signal
ECCC	Environment and Climate Change Canada
ECMWF	European Centre for Medium-Range Weather Forecasts
FIR	Far infrared
FIRR	Far InfraRed Radiometer
FIRST	Far-Infrared Spectroscopy of the Troposphere
FORUM	Far Infrared Outgoing Radiation Understanding and Monitoring
HIRS	High resolution Infrared Radiation Sounder
HSB	Humidity Sounder for Brazil
IASI	Infrared Atmospheric Sounding Interferometer
IASI-NG	IASI- Next Generation
IGRA	Integrated Global Radiosonde Archive
IR	Infrared
IRIS	Infrared Interferometer Spectrometer and Radiometer
METOP	Meteorological Operational satellite
MIR	Mid-infrared
MODTRAN	MODerate resolution atmospheric TRANsmission
MODIS	Moderate Resolution Imaging Spectroradiometer
NER	Noise Equivalent Radiance
NETCARE	Network on Climate and Aerosols: Addressing Key Uncertainties in Remote Canadian Environments
NETD	Noise-equivalent temperature difference

OSE	Observing System Experiment
OSSE	Observing System Simulation Experiment
PNT	Prévision Numérique du Temps
PREFIRE	Polar Radiant Energy in the Far InfraRed Experiment
REFIR	Radiation Explorer in Far-Infrared
RTTOV	Radiative Transfer for TOVS
TAFTS	Tropospheric Airborne Fourier Transform Spectrometer
TICFIRE	Thin Ice Clouds in Far InfraRed Experiment
TIROS	Television Infra-Red Observation Satellite
TOA	Top Of the Atmosphere
TOVS	TIROS Operational Vertical Sounder
UTLS	Upper Troposphere/Lower Stratosphere

RÉSUMÉ

Une nouvelle génération d'instruments mesurant dans l'infrarouge thermique et à haute résolution spectrale, soit Atmospheric Infrared Sounder (AIRS) (Aumann et al., 2003), Infrared Atmospheric Sounding Interferometer (IASI) (Blumstein et al., 2004) et Cross-track Infrared Sounder (CrIS) (Bloom, 2001), apporta son lot de recherche pour trouver une sélection optimale d'un sous-ensemble de canaux contenant le plus d'information possible. Plusieurs méthodes furent testées afin de trouver une méthode optimale d'un point de vue de l'assimilation de données (Rabier et al., 2002). Les principales méthodes retenues sont une méthode itérative utilisant le contenu en information et la méthode des Jacobiens (basée sur les caractéristiques des Jacobiens). Ils conclurent que la méthode itérative donnait de meilleurs résultats en termes de réduction de l'erreur d'analyse comparativement à la méthode des Jacobiens, mais qu'elle était plus coûteuse au niveau du temps de calcul. Cette thèse s'intéresse à cette méthode itérative utilisant le contenu en information pour la sélection de canaux pour des instruments satellitaires mesurant dans l'infrarouge thermique et lointain. Le DFS (Degrees of Freedom per signal) fut utilisé dans une première étude pour optimiser un radiomètre mesurant dans l'infrarouge lointain en termes du nombre de bandes et de leur largeur spectrale pour l'Arctique. Une configuration optimale a été trouvée, composée de 22 bandes pour la température et 7 bandes pour l'humidité. Ces mesures apportent de l'information complémentaire à AIRS pour l'humidité, entre la surface et 850 hPa et entre 550 hPa et 250 hPa. Individuellement, les mesures dans l'infrarouge lointain permettent de réduire la variance de l'erreur d'analyse entre 400 hPa et 200 hPa mieux que AIRS par rapport à l'humidité. Cette recherche permit de démontrer le potentiel de mesures dans l'infrarouge lointain pour améliorer l'analyse de l'humidité dans l'Arctique. La deuxième étude utilise la même technique itérative pour trouver une sélection optimale de canaux pour l'instrument CrIS. Ainsi, une configuration optimale composée de 455 canaux a été trouvée. Par la suite, cette configuration a été comparée avec celle de Carminati (2022) composée de 431 canaux. Même si les deux configurations ont 224 canaux identiques, les résultats en termes de réduction d'erreur d'analyse sont similaires. La différence d'erreur d'analyse sommée sur le profil atmosphérique entre les deux configurations est égale à 7.4 K^2 and 0.077 $(logLL^{-1})^2$ (où L L^{-1} represents le ratio volumique de la vapeur d'eau sur le volume d'air). Différentes matrices de covariances d'erreur d'observation ont été prises pour évaluer l'effet de cette matrice sur la sélection

de canaux. Même si les canaux sélectionnés sont différents pour les différentes matrices, les résultats en termes d'erreur d'analyse sont similaires. Un aspect intéressant de cette thèse est l'utilisation de la méthode itérative qui permet de facilement tester différentes configurations d'un instrument autant au niveau du nombre de canaux qui devraient être assimilés que pour trouver une configuration optimale en termes de largeur spectrale et du nombre de bandes dépendant des variables étudiées. De plus, cette méthode itérative utilisant le DFS permet de trouver un nombre optimal de canaux qui devraient être assimilés pour les centres de prévisions numériques du temps (PNT) et de trouver une sélection de canaux meilleure qu'avec la méthode des Jacobiens.

Mots-clés: Infrarouge lointain, CrIS, contenu en information, erreur d'analyse, sélection optimale de canaux, optimisation des bandes

INTRODUCTION

Depuis l'avènement des satellites météorologiques, les mesures de radiance dans l'infrarouge (IR) particulièrement dans la bande d'absorption à 15 μm ont été utilisées pour faire du profilage de température (Wark & Hilleary, 1969). Les instruments TIROS Operational Vertical Sounder (TOVS) ont fourni les premières données de radiances satellitaires permettant d'obtenir des analyses des profils de température et d'humidité aux centres de prévision numérique du temps (PNT) (Smith, 1979) au début des années 1980. Il fut démontré à l'aide d'Observing system experiment (OSE), qui consiste à réaliser deux expériences d'assimilation en parallèle, une en incluant et l'autre en excluant un type de données, que ces données avaient un impact positif sur les prévisions de température dans l'hémisphère sud tandis que l'impact de ce type d'observations pour l'hémisphère nord était dépendant des conditions météorologiques et synoptiques (Andersson et al., 1991). Cependant, ces données avaient une faible résolution verticale et une faible précision (une incertitude de 2 K pour la température et entre 20 et 30 % pour l'humidité). De plus, ces données n'étaient pas assimilées directement; elles étaient utilisées pour générer des profils de température et d'humidité qui étaient par la suite assimilés. Cette inversion utilisant la même prévision que l'assimilation, l'erreur de ces données ne sont plus indépendantes de celles de la prévision. L'utilisation de données brutes évite ce problème. L'utilité d'assimiler directement les radiances de TOVS fut démontré et aussi, qu'il y avait un impact positif pour les PNT dans les hémisphères nord et sud (Eyre et al., 1993). Il a été démontré que la variation de transmittance de la bande de CO_2 à 4.3 μm pouvait aussi être utilisée pour caractériser la structure verticale de la température (Ka-

plan et al., 1977). Ceci amena, entre autres, une nouvelle génération d'instruments mesurant dans l'infrarouge thermique et à haute résolution spectrale, soit Atmospheric Infrared Sounder (AIRS) (Aumann et al., 2003), Infrared Atmospheric Sounding Interferometer (IASI) (Blumstein et al., 2004) et Cross-track Infrared Sounder (CrIS) (Bloom, 2001). Les caractéristiques physiques et les objectifs de mesures de ces instruments seront brièvement discutés dans les sections suivantes. On s'intéressera également au potentiel de canaux dans l'infrarouge lointain pour caractériser la structure verticale de la température et de l'humidité.

1.1 Description des principaux sondeurs satellitaires hyperspectraux dans l'infrarouge

1.1.1 AIRS

L'instrument satellitaire AIRS de la NASA, qui est à bord du satellite Aqua fut lancé en 2002 et fut le premier de cette catégorie d'instruments hyperspectraux. Deux autres instruments sont à bord de ce satellite, soit AMSU (Advanced Microwave Sounding unit) et HSB (Humidity Sounder for Brazil) et sont opérés de manière synchrone avec AIRS. AIRS est un spectromètre mesurant entre 3.7 et 15.4 μm avec 2378 bandes dans cet intervalle avec une résoltion spectrale entre 0.5 et 2 cm^{-1} dépendant des régions. Avec ces trois instruments, il est possible d'obtenir les propriétés nuageuses, des profils atmosphériques de température et d'humidité, la température de surface pour l'océan et du sol. Lorsque ce satellite a été construit, il avait donc comme objectifs d'améliorer les PNT et de contribuer aux études climatiques vu sa précision de 1 K pour une une couche moyenne d'une épaisseur de 1 km pour l'inversion de température et une précision de 10 % pour une épaisseur de 2 km dans la troposphère pour l'humidité (Aumann et al., 2003). De plus, ce qui rend AIRS intéressant, est sa capacité à mesurer la vapeur d'eau dans la haute troposphère, vu que les mesures traditionnelles, soit les radiosondes,

sont incapables de fournir de bonnes mesures dans cette région. Cette région tend à avoir un biais sec dans les modèles globaux (Sherwood et al., 2010). De plus, un des avantages des données satellitaires est leur couverture globale contrairement aux radiosondages qui ne couvrent principalement que les régions terrestres (Durre et al., 2005).

1.1.2 IASI et IASI-NG

L'instrument IASI est à bord du satellite à orbite polaire européen Metop. Il fut mis en orbite en 2006. IASI est un spectromètre à transformée de Fourier et est basé sur un interféromètre de Michelson. C'est un instrument de télédétection passive mesurant dans l'infrarouge thermique, soit de 3.7 à 15.5 μm avec une résolution spectrale de 0.25 cm^{-1}. Ainsi, il possède 8461 canaux. L'objectif principal de cet instrument est d'obtenir des profils atmosphériques de température avec une erreur de 1 K pour une couche de 1 km, d'obtenir des profils d'humidité avec une précision de 10 % pour une couche de 1 km et aussi de récupérer des quantités de gas traces totaux dans une colonne (Blumstein et al., 2004). De plus, l'instrument fournit également de l'information sur les gas traces à effet de serre, sur la température de surface et les propriétés nuageuses avec des mesures de la température de la surface de l'océan, la température du sol et son émissivité, la transmittance des nuages et la réflectance. De plus, l'instrument s'est montré d'une grande utilité pour mesurer la composition chimique de l'atmosphère. Des distributions globales de plusieurs gaz traces sont maintenant possibles avec IASI ainsi que des distributions locales de molécules organiques durant les feux de forêt (Clerbaux et al., 2009). Ainsi, à cause de sa grande contribution à l'amélioration des PNT et dans la surveillance de la qualité de l'air et du climat, une nouvelle génération de l'instrument sera mise en orbite en 2025. L'instrument IASI-NG (IASI-New Generation) a de meilleures caractéristiques radiométriques et spectrales compar-

ativement à IASI. L'instrument mesure dans le même intervalle spectral, mais avec une résolution plus fine à 0.125 cm^{-1}. De plus, l'instrument possède 16 921 canaux, soit le double de IASI. Cette nouvelle génération de l'instrument IASI permet une meilleure couverture verticale dans la basse troposphère ainsi qu'une augmentation de la précision pour le profilage de plusieurs variables thermodynamiques, climatiques et chimiques (Crevoisier et al., 2014).

1.1.3 CrIS

L'instrument CrIS fut lancé en 2011. Il s'agit d'un spectromètre à transformée de Fourier ayant 2211 bandes. L'instrument mesure dans trois bandes, soit 9.13-15.26 μm, 5.71-8.26 μm et 3.92-4.64 μm avec des résolutions spectrales de 0.625 cm^{-1}, 1.25 cm^{-1} et 2.5 cm^{-1} respectivement (Bloom, 2001). L'instrument CrIS a pour objectif de résolution d'avoir une incertitude de 1.0 K par couche de 1 km pour la température et une incertitude de moins de 15 % par couche de 2 km dans la troposphère pour la vapeur d'eau (Bloom, 2001). Cet instrument correspond au second spectromètre à transformée de Fourier qui fut déployé pour les PNT après IASI (Han et al., 2013). Il a d'ailleurs une couverture spectrale similaire à AIRS, mais plus petite que IASI (Smith et al., 2015). Similairement aux instruments précédents, cet instrument a pour but de fournir des données de température et d'humidité précises afin d'améliorer les prévisions météorologiques à court et moyen terme et les simulations climatiques.

1.1.4 L'infrarouge lointain

Il fut démontré que les bandes pouvant être utilisées pour faire du profilage atmosphérique sont les bandes d'absorption du dioxide de carbone à 4.3μm et à 15 μm, à cause de la variation de la transmittance dans ces parties du spectre

(Wark & Hilleary, 1969). Pourtant, il y une autre région qui possède une variation semblable de la transmittance, soit l'infrarouge lointain (FIR ; $15\mu m < \lambda < 100$ μm) qui est dû à une bande d'absorption rotationnelle de la vapeur d'eau et au continuum. Cette bande d'absorption est plus large que la bande d'absorption vibrationnelle, et ainsi, il y a plus d'énergie dans cette région.

Des études ont montré le potentiel de l'infrarouge lointain pour profiler l'atmosphère, particulièrement les régions froides (Mlynczak et al., 2004). Premièrement, conséquence directe de la dépendance de la fonction de Planck à la température dans l'équation du transfert radiatif, la radiance émise est décalée vers l'infrarouge lointain quand la température décroît. Cette caractéristique offre une grande capacité aux scènes froides à être sondéees (Mlynczak et al., 2007), contrairement à la bande traditionnelle à 6.3 μm qui perd de l'énergie rapidement (Susskind et al., 2003).

Ainsi, plus de la moitié de la radiation perdue dans l'espace est dans l'infrarouge lointain pour les régions polaires (Mlynczak et al., 2007). Deuxièmement, la bande d'absorption rotationnelle de la vapeur d'eau dans l'infrarouge lointain a plusieurs lignes d'absorption ayant une épaisseur optique plus grande que dans l'infrarouge thermique, ce qui conduit à une augmentation de la sensibilité à de faibles variations de vapeur d'eau (Harries et al., 2008). Cette augmentation de la sensibilité est particulièrement importante dans la haute troposphère, où les concentrations de vapeur d'eau sont minimes (Clough et al., 1992). Ainsi, l'infrarouge lointain peut être utile pour profiler l'atmosphère et particulièrement la stratosphère et la haute troposphère (Shahabadi & Huang, 2014).

Au cours de la dernière décennie, quelques projets de mesures dans l'infrarouge lointain à partir du sol dans des régions sèches, froides ou élevées ont été réalisés internationalement. Il y a le Radiation Explorer in Far-Infrared (REFIR)

par un consortium européen (Carli et al., 1999), le Far-Infrared Spectroscopy of the Troposphere (FIRST) développé par la NASA (Mlynczak et al., 2004) et le Tropospheric Airborne Fourier Transform Spectrometer (TAFTS) développé à l'Imperial College de Londres (Canas et al., 1997). Ces instruments ont une résolution spectrale variant entre 0.1 et 0.6 cm^{-1}. Ces projets ont différents objectifs scientifiques. Celui de REFIR est d'étudier les propriétés radiatives de la vapeur d'eau et des cirrus dans la partie supérieure de la troposphère tandis que celui de FIRST est de contraindre le budget énergétique de l'atmosphère globalement de manière journalière. TACTS a comme objectif de calculer les flux radiatifs nets et la divergence de flux (taux de croissance ou décroissance de la radiation).

Le projet REFIR, renommé FORUM pour Far Infrared Outgoing Radiation Understanding and Monitoring (Palchetti et al., 2016), comprend un projet satellitaire pour étudier les forçages et rétroactions de la vapeur d'eau atmosphérique sous la forme de vapeur et de nuages sur le climat. Le projet FIRST possède également une mission satellitaire, le Climate Absolute Radiance and Refractivity Observatory (CLARREO) (Wielicki et al., 2013). CLARREO mesurera le spectre d'émission de la Terre entre 5 - 50 μm avec une fine résolution spectrale afin de détecter les changements décennaux des forçages, réponses et rétroactions du climat de même que pour servir de référence pour l'intercalibration. Vu que son objectif est de prendre des mesures annuelles ou sur de plus longues échelles temporelles, son niveau de bruit, la différence de température équivalente de bruit (NETD), a pour seule contrainte d'être inférieure à 10 K dans l'infrarouge lointain, valeur trop grande pour extraire un profil de vapeur d'eau atmosphérique. À titre de comparaison, le NETD de AIRS est environ de 1 K (Aumann et al., 2003).

Les instruments au sol, REFIR, TACTS et FIRST ainsi que les études sur la valeur ajoutée de mesures dans l'infrarouge lointain par rapport à la température et l'humidité sont basés sur des interféromètres. Cependant, utiliser un

radiomètre au lieu d'un interféromètre pour mesurer dans l'infrarouge lointain permet d'avoir des bandes larges dans l'infrarouge lointain et des bandes plus fines dans l'infrarouge thermique en utilisant des filtres différents. Un radiomètre au sol mesurant dans l'infrarouge lointain existe, soit le Far InfraRed Radiometer (FIRR) (Libois et al., 2016b). C'est un prototype pour la mission satellitaire Thin Ice Clouds in Far InfraRed Experiment (TICFIRE). L'objectif de cet instrument est de mesurer la radiance émise par la Terre et son atmosphère dans l'infrarouge lointain avec un intérêt particulier pour les nuages de glace optiquement minces et la vapeur d'eau dans les régions froides (polaires et UTLS (Upper Troposphere/Lower Stratosphere)). Des mesures aéroportées avec l'instrument ont été prises en Arctique lors de la campagne NETCARE afin de tester la technologie dans des conditions similaires à des observations satellitaires au nadir (Libois et al., 2016a). Libois & Blanchet (2017) ont analysé le potentiel de mesures dans l'infrarouge lointain pour la télédétection de nuages de glace. Ils conclurent qu'ajouter quelques bandes dans l'infrarouge lointain à des radiomètres satellitaires tel que MODIS pourrait améliorer considérablement le recouvrement des propriétés radiatives des nuages de glace (Libois & Blanchet, 2017).

1.2 Problématique avec ce type de mesures satellitaires

Les instruments hyperspectraux satellitaire amenèrent un nouveau défi pour les centres de PNT. En effet, il n'est pas réalisable ni efficace d'assimiler l'intégralité des bandes de ces instruments ni d'extraire des profils atmosphériques de ces mesures pour ensuite les assimiler. Des techniques utilisant l'assimilation de données furent donc introduites afin de trouver un sous-ensemble de bandes contenant le maximum d'information.

Rodgers (1998) montra l'utilité d'utiliser le contenu en information, qui est une

mesure du degré d'indépendance des observations et considère le niveau de redondance. (Purser & Huang, 1993) pour identifier un sous-ensemble de canaux qui contribue le plus au contenu en information pour une mesure donnée. Ils ont utilisé cette approche pour identifier un tel sous-ensemble de canaux de l'instrument AIRS. Il s'agit d'une méthode d'évaluation basée sur les erreurs relatives entre les observations et l'information *a priori*. La technique utilisée par Rodgers (1998) est de calculer le contenu en information pour chacune des bandes individuellement, de sélectionner celle ayant le plus grand contenu en information et de calculer le contenu en information de chacune de bandes restantes une fois ajoutée à celle sélectionnée précédemment. Ce processus est fait de manière itérative pour ordonner les bandes et optimiser quelles bandes choisir. Les différentes études qui ont été faites sur la sélection de canaux pour les instruments précédemment mentionnés soit AIRS, IASI, CrIS et dans l'infrarouge lointain seront résumé dans les prochains paragraphes.

1.2.1 IASI

Plusieurs méthodes ont été testées par Rabier et al. (2002) pour la sélection de canaux de l'instrument IASI. Les deux méthodes donnant les meilleurs résultats sont la méthode itérative mentionnée plus haut et la méthode des Jacobiens. Cette dernière utilise les caractéristiques du modèle de transfert radiatif en calculant les variations de radiance en fonction de perturbations aux profils atmosphériques, soit les Jacobiens pour obtenir une bonne couverture verticale. Avec la méthode itérative, le contenu en information total est plus grand que pour la méthode des Jacobiens pour un sous-ensemble de 300 canaux. D'ailleurs, Rabier et al. (2002) notèrent qu'étant donné que la sélection de canaux ne peut être faite pour chaque profil atmosphérique, ce qui serait trop long et coûteux dans un cadre opérationnel, une sélection de canaux construite avec un sous-ensemble de profils et moyennée

sur ces profils est une solution adéquate. Il a été montré qu'il y a une perte minime du contenu en information en utilisant cette méthode moyennée pour la sélection itérative tandis que pour la méthode des Jacobiens, dite physique, la diminution du contenu en information est plus grande. La méthode itérative moyennée est donc appropriée pour être utilisée pour la sélection de bandes d'un instrument dans les centres de PNT.

Collard & McNally (2009) identifièrent à l'aide de la méthode de Rabier et al. (2002) un ensemble de 300 canaux qui sera transmis aux centres de PNT. Une matrice de covariances d'erreurs d'observations diagonale composée de l'erreur de mesure et de 0.2 K pour inclure l'erreur de représentativité fut utilisée (Collard & McNally, 2009). Noh et al. (2017) firent par la suite une comparaison de la sélection de Collard (2009) avec une sélection de canaux utilisant un indice de pointage par canaux avec des Jacobiens changeant avec les itérations d'un modèle 1D. Environ les trois quarts des canaux sont identiques en comparaison avec la sélection de (Collard & McNally, 2009) et les autres canaux proviennent de la bande de vapeur d'eau (Noh et al., 2017). Ces nouveaux canaux ont permis de réduire le biais dans la haute troposphère dans les analyses. Coopmann et al. (2020) comparèrent eux aussi la sélection de Collard (2009), mais cette fois-ci avec une matrice de covariances d'erreur d'observations complète. Ils démontrèrent qu'avec une matrice de covariances d'erreur d'observations complète et non diagonale, l'erreur sur l'analyse est diminuée de 3% pour la température, 1.8% pour l'humidité et 0.9% pour l'ozone en moyenne comparé avec la sélection de canaux précédente (Coopmann et al., 2020).

En prévision de la nouvelle génération de l'instrument IASI, (IASI-NG), Vittorioso et al. (2021) utilisèrent lecontenu en information pour sélectionner 500 canaux pour la température et l'humidité. Une matrice de covariance d'erreur d'observations complète fut utilisée en utilisant la méthode de (Desroziers et al.,

2005). L'impact de cette sélection fut mesurée avec la réduction de l'écart type sur l'erreur d'analyse de la température et l'humidité par rapport à l'a priori. Il y a une réduction de l'erreur jusqu'à 30% pour la température et jusqu'à 50 % pour l'humidité (Vittorioso et al., 2021).

1.2.2 AIRS

Fourrié & Thépaut (2003) testèrent les deux approches proposées par Rabier (2002), soit la sélection de canaux avec les Jacobiens (Susskind et al., 2003) et la méthode itérative avec l'instrument AIRS et en faisant ce calcul pour un ensemble de 108 profils atmosphériques regroupés en trois catégories, soit tropical, latitudes moyennes et polaires. Un sous-ensemble de 324 canaux fut sélectionné pour la méthode itérative ayant un DFS plus grand que pour la méthode des Jacobiens (Fourrié & Thépaut, 2003).

Joiner et al. (2007) testèrent l'impact de l'erreur d'observation sans tenir compte des corrélations spectrales ou spatiales sur la sélection de canaux et aussi sur la précision des prévisions météorologiques. Leur expérience consistait à inclure et exclure la bande de H_2O entre 1080 et 1610 cm^{-1}. Pour les deux hémisphères nord et sud, exclure la bande d'H_2O avec une petite erreur d'observation a le plus grand impact positif sur les prévisions. Cette expérience démontre ainsi l'importance d'exclure certaines bandes et que de les prévisions sont influencées par l'erreur d'observation (Joiner et al., 2007) .

1.2.3 CrIS

Gambacorta & Barnet (2012) ont fait une première étude pour sélectionner un sous-ensemble de canaux pour l'instrument CrIS. Avec la méthode des Jacobiens, 173 canaux furent sélectionnés et vérifiés avec 4000 profils répartis uniformément

entre des scènes d'océan, de sol et de nuit et de jour. Cependant, cette sélection est basée sur trois critères, soit la pureté du signal des canaux, c'est-à-dire la sensibilité d'un canal à un nombre restreint de composantes atmosphériques, la résolution verticale et les canaux ayant une erreur de mesure minimale (Gambacorta & Barnet, 2012). Même si l'objectif de cette sélection n'a pas été fait pour les centres de PNT, Smith et al. (2015) analysèrent la qualité des mesures provenant de cette sélection en comparant les observations au modèle. En assimilant ces mesures, l'erreur de prévision est réduite modestement (Smith et al., 2015).

Carminati (2022) calculèrent une nouvelle sélection de canaux où la priorité est mise sur une sélection faite pour réduire les covariances d'erreur d'analyse, donc de trouver une sélection optimale pour les centres de PNT. Ainsi avec 80 différents profils atmosphériques et une matrice $\mathbf{R}$ calculée en utilisant la méthode de (Desroziers et al., 2005), une sélection de 431 canaux a été obtenue. Le contenu en information pour la température de surface a très peu d'impact, tandis que ceux de la température et de l'humidité sont positifs. En effet, le contenu en information pour ces deux variables augmente jusqu'à ce que 400 canaux soient sélectionnés (Carminati, 2022).

1.2.4 Infrarouge lointain

Des études sur la faisabilité d'utiliser des interféromètres satellitaires dans l'infrarouge lointain pour restituer des profils de température et d'humidité ont été réalisées. Une étude a utilisé les caractéristiques de CLARREO pour modéliser deux interféromètres, soit l'un mesurant dans l'infrarouge moyen (MIR) et l'autre mesurant dans l'infrarouge lointain (FIR) (Merrelli & Turner, 2012). Il a été démontré que le senseur FIR possède plus de contenu en information et a une meilleure résolution verticale pour la vapeur d'eau comparé au senseur MIR pour le même niveau

de bruit. Cependant, il est attendu que le niveau de bruit pour CLARREO sera plus élevé et, dans ces conditions, l'avantage des mesures dans l'infrarouge lointain est négligeable par rapport aux mesures dans l'infrarouge thermique.

Une autre étude a analysé la capacité à restituer l'humidité stratosphérique d'un interféromètre dans l'infrarouge lointain au niveau de la tropopause. Leur première expérience a démontré qu'inclure l'infrarouge lointain est essentiel pour récupérer avec précision la concentration de vapeur d'eau avec un niveau de bruit comparable à celui de CLARREO (Shahabadi & Huang, 2014). Leur deuxième expérience, cette fois avec des senseurs réels ayant donc un niveau de bruit plus élevé, conclut qu'augmenter la précision dans l'infrarouge lointain au même niveau que l'infrarouge thermique n'améliore pas la reconstruction de la vapeur d'eau (Shahabadi et al., 2015). Ainsi, ces études montrent que la valeur ajoutée de mesures dans l'infrarouge lointain est dépendante du niveau de bruit de l'instrument.

Il est important de comprendre que toutes les études sur le contenu en information sont dépendantes des hypothèses qui ont été faites par rapport aux erreurs de prévision, aux erreurs d'observations et au modèle de transfert radiatif choisi ainsi que la région géographique considérée.

1.3 Objectifs de recherche

Les objectifs de recherche sont séparés en deux parties, traitent toutes deux de la sélection de canaux et du contenu en information pour les instruments satellitaires. La première partie de la thèse porte sur la sélection de canaux en fonction du DFS pour un radiomètre mesurant dans l'infrarouge lointain avec une méthode itérative et ainsi d'évaluer l'impact de ces mesures dans un contexte d'assimilation de données en une dimension. Un modèle 1D vertical situé à plusieurs endroits en Arctique, pour lesquels on utilise une matrice B représentative de la région

arctique, est utilisée. La deuxième partie de cette recherche utilise cette même technique itérative pour faire une sélection de canaux, mais pour l'instrument CrIS et ainsi permet de comparer cette méthode à celle déjà utilisée à Environnement et Changements climatique Canada (ECCC) soit celle des Jacobiens.

Le spectromètre que l'on considère est un instrument synthétique, ayant le bruit radiométrique de l'instrument FIRR (Libois et al., 2016b). Le premier objectif de cette recherche était de trouver une configuration optimale pour l'instrument par rapport au nombre de bandes et la largeur spectrale de celles-ci. Une fois que la configuration optimale de l'instrument fut trouvée, une sélection des bandes est faite comme ce qui a été fait précédemment (Rabier et al., 2002) (Fourrié & Thépaut, 2003) Ainsi, un sous-ensemble de canaux est obtenu et qui apporte le plus d'information possible pour la température et l'humidité, les deux variables considérées dans cette étude. Pour évaluer l'impact de ce nouveau type de mesures, le contenu en information de la configuration optimale est calculé et comparé à celui de AIRS. Il est important de comparer avec des mesures déjà existantes, car dans les centres de PNT, aucune mesure n'est considérée individuellement. De plus, pour voir l'impact vertical d'assimiler ces mesures, l'erreur d'analyse est utilisée. Cette première étude a été faite sur l'Arctique vu qu'il y a plus d'énergie dans l'infrarouge lointain lorsque la température est faible et que l'instrument FIRR a déjà été déployé à Eureka, Canada (S Pelletier et al., 2017).

En deuxième partie, on s'intéresse à l'instrument CrIS. Normalement, dans les centres opérationnels de PNT, la sélection des bandes est faite avec les Jacobiens, en sélectionnant ceux ayant un sommet plus pointu et n'ayant pas de lobes latéraux et qui sondent à différentes altitudes. Cependant, comme mentionné précédemment, cette méthode, soit celle des Jacobiens, n'est pas celle donnant les meilleurs

résultats. Ainsi, une nouvelle sélection a été faite en utilisant le contenu en information pour avoir une sélection moyennée globalement pour l'instrument CrIS. Ce nouveau sous-ensemble de bandes a été, par la suite, comparé avec la sélection initiale ainsi qu'avec la sélection faite par Carminati (2022) afin d'analyser les canaux sélectionnés par les différentes études. De plus, l'erreur d'analyse a été utilisée pour voir l'impact vertical de ces configurations. Finalement, pour une région donnée, différentes matrices de covariances d'erreurs d'observations ont été considérées afin d'évaluer l'impact sur la sélection de canaux de cette matrice. Cette recherche pour l'instrument CrIS est faite en collaboration avec l'équipe d'assimilation de données à ECCC.

CHAPITRE II

MÉTHODOLOGIE

2.1 Assimilation de données

Comme mentionné précédement dans l'introduction, des techniques utilisant l'assimilation de données sont utilisées afin de trouver un sous-ensemble de bandes contenant le maximum d'information. Ainsi, le cadre théorique sera introduit permettant de mieux comprendre les techniques utilisées pour effectuer la sélection des bandes.

L'assimilation de données est basée sur l'estimation statistique d'erreurs dans le cadre de la prévision météorologique (Rodgers, 2000). Les différentes notations, définitions, approximations et les données utilisées seront décrites ci-dessous.

L'état de l'atmosphère est représenté par un vecteur $\mathbf{x}$ et les observations assimilées par le vecteur $\mathbf{y}$. Les observations comprennent des données provenant de différents types d'instruments, allant de radiosondages aux radiances satellitaires. Les observations sont reliées à l'état de l'atmosphère par l'opérateur $\mathrm{H}(\mathbf{x})$. Ceci permet une comparaison directe de toutes les observations à leur équivalent modèle via l'équation suivante

$$\mathbf{y} = H(\mathbf{x}) + \epsilon_o, \tag{2.1}$$

où ϵ_o est l'erreur d'observation. Dans le cadre de ces recherches, l'état de l'atmosphère correspond aux profils de température, $\mathbf{T}$, et d'humidité $\mathbf{q}$ défini sur k niveaux verticaux sur lequel l'état modèle $\mathbf{x}$ est défini. La dimension de l'état modèle $\mathbf{x}$ est donc 2k. L'ozone et les autres gaz traces sont considérés constants. L'assimilation cherche à corriger un estimé *a priori* de l'état de l'atmosphère, $\mathbf{x_b}$ en utilisant l'information contenue dans les observations. L'assimilation prend en considération les précisions relatives de $\mathbf{x}$ et $\mathbf{y}$ afin d'obtenir un estimé ayant une variance minimale, $\mathbf{x_a}$, appelé analyse.

Une linéarisation du modèle autour du profil atmosphérique, $\mathbf{x}_b$, est faite ce qui donne, en supposant que l'équation du transfert radiatif est faiblement nonlinéaire près de l'état modèle

$$H(\mathbf{x}) \cong H(\mathbf{x}_b) + \mathbf{H}(\mathbf{x} - \mathbf{x}_b), \tag{2.2}$$

où $H(\mathbf{x}_b)$ est l'ébauche représentée dans l'espace des observations et $\mathbf{H} = \left.\frac{\partial H(x)}{\partial x}\right|_{x_b}$ est l'opérateur d'observations linéarisé par rapport à $\mathbf{x}$ évalué à $\mathbf{x} = \mathbf{x}_b$, appelé Jacobien.

L'analyse, $\mathbf{x}_a$, qui représente l'état de l'atmosphère corrigé en considérant les observations et le modèle est déterminé par

$$\mathbf{x}_a = \mathbf{x}_b + \mathbf{K}(\mathbf{y} - \mathbf{H}\mathbf{x}_b) \tag{2.3}$$

où $\mathbf{K} = \mathbf{B}\mathbf{H}^T(\mathbf{R}+\mathbf{H}\mathbf{B}\mathbf{H}^T)^{-1}$ est la matrice de gain obtenue en minimisant la variance de l'erreur d'analyse totale en considérant la covariance d'erreur de prévision $\mathbf{B}$ ainsi que celle de l'erreur d'observation $\mathbf{R}$. Les symboles T et -1 indiquent, respectivement, la transposée et l'inverse d'une matrice. La matrice de gain dépend également de l'opérateur d'observation linéarisé, $\mathbf{H}$, au voisinage de x_b. Cette linéarisation permet d'écrire l'impact d'un changement à la variable d'état de l'ordre de ϵ_b sur l'écart à l'observation donné par l'équation 2.1.

2.2 Contenu en information

L'impact de mesures est estimé avec la matrice de covariance d'erreur d'analyse et le contenu en information (DFS *degrees of freedom per signal*). L'erreur d'analyse, supposée sans biais, est $\varepsilon_a = \mathbf{x}_a - \mathbf{x}_t$ où $\mathbf{x}_t$ est considéré comme l'état réel de l'atmosphère. Donc, $\mathbf{A} = \langle \varepsilon_a \varepsilon_a^T \rangle$, $\langle ... \rangle$ étant la moyenne statistique, est la matrice de covariance de l'erreur d'analyse et on peut montrer que

$$\mathbf{A} = (\mathbf{I} - \mathbf{K}\mathbf{H})\mathbf{B}. \tag{2.4}$$

La réduction de l'erreur d'analyse est due à l'assimilation d'observations et est mesurée par

$$tr(\mathbf{A}\mathbf{B}^{-1}) = N - tr(\mathbf{K}\mathbf{H}), \tag{2.5}$$

où $tr(\mathbf{K}\mathbf{H}) = tr(\mathbf{H}\mathbf{K})$. Le gain en information (DFS) est défini par

$$\text{DFS} = tr(\mathbf{HK}). \tag{2.6}$$

Le DFS peut être vu de deux manières, dans l'espace des observations ou dans l'espace modèle. Dans l'espace des observations, le DFS mesure le degré d'indépendance des observations et considère ainsi le niveau de redondance. Dans l'espace modèle, le DFS mesure la réduction de l'erreur d'analyse par rapport à l'erreur initiale de prévision.

Le DFS est une méthode d'évaluation basée sur les erreurs relatives entre les observations et l'information *a priori* (Purser & Huang, 1993). Le DFS a aussi été utilisé pour quantifier la valeur ajoutée d'un nouveau type d'observations en comparant d'autres types de mesures et aussi lorsqu'ajouté à des mesures déjà assimilées (McNally et al., 2006; Lupu et al., 2011).

Ainsi, la matrice de covariance d'erreurs d'analyse $\mathbf{A}$ et le DFS dépendent de la matrice de covariance d'erreurs de prévision, la matrice de covariance d'erreur d'observation $\mathbf{R}$ et de la matrice de Jacobiens $\mathbf{H}$. L'impact d'un type d'observations peut être quantifié en comparant deux expériences, l'une dans laquelle toutes les observations sont assimilées et l'autre où un type d'observation est retiré des données assimilées. La différence de variance d'erreur est une mesure de la réduction apportée par ce type d'observation et mesure donc la valeur ajoutée par ce nouveau type d'observation.

CHAPITRE III

OPTIMAL CONFIGURATION OF A FAR-INFRARED RADIOMETER TO STUDY THE ARCTIC WINTER ATMOSPHERE

Ce chapitre présente un article qui a été publié dans le *Journal of Geophysical Research: Atmospheres* (publié le 8 juin 2020):

Coursol, L., Libois, Q., Gauthier, P., & Blanchet, J. P. (2020). Optimal configuration of a far-infrared radiometer to study the Arctic winter atmosphere. *Journal of Geophysical Research: Atmospheres*, 125(14), e2019JD031773.

Une étude théorique est faite afin d'aider à la conception d'un radiomètre mesurant dans l'infrarouge lointain, où la configuration est optimisée avec le contenu en information pour le nombre de canaux ainsi que la largeur spectrale de ceux-ci. L'étude est faite dans un contexte en une dimension pour déterminer la configuration optimale de l'instrument mesurant dans l'infrarouge lointain pour étudier la nuit polaire en Arctique. Pour obtenir 90 % de l'information disponible, 4 bandes sont nécessaires pour l'humidité tandis que 10 bandes sont requises pour la température. Lorsque les mesures dans le FIR sont assimilées complémentairement à celles de AIRS, il y a de l'information additionnelle entre la surface et 850 hPa et entre 550 et 250 hPa pour l'humidité. De plus, entre 400 et 200 hPa, les mesures

dans le FIR sont meilleures pour réduire l'erreur d'analyse comparativement à AIRS pour l'humidité.

Optimal configuration of a far-infrared radiometer to the study the Arctic winter atmosphere

Laurence Coursol[1], Quentin Libois[2], Pierre Gauthier [1] and Jean-Pierre Blanchet [1]

[1] Université du Québec à Montréal (UQAM), Montréal, Canada

[2] CNRM, Université de Toulouse, Météo-France, CNRS, Toulouse, France

[1] Corresponding author: Laurence Coursol, laurence.coursol@gmail.com

Abstract

Several FIR satellite missions are planned for the next decade, with a special interest for the Arctic region. A theoretical study is performed to help about the design of a FIR radiometer, whose configuration in terms of channels number and frequencies is optimized based on information content analysis. The problem is cast in a context of vertical column experiments (1D) to determine the optimal configuration of a FIR radiometer to study the Arctic polar night. If only observations of the FIR radiometer were assimilated, the results show that for humidity, 90 % of the total information content is obtained with 4 bands whereas for temperature 10 bands are needed. When the FIR measurements are assimilated on top of those from the Advanced Infrared Sounder (AIRS), the former bring in additional information between the surface and 850 hPa and from 550 hPa to 250 hPa for humidity. Moreover, between 400 hPa and 200 hPa, the FIR radiometer is better than AIRS at reducing the analysis error variance for humidity. This indicates the potential of FIR observations for improving water vapor analysis in the Arctic.

Keypoints: FIR channels add information for UTLS water vapor compared to standard MIR channels. IC is used to optimize the channels frequencies and widths of a FIR radiometer. A high DFS is reached with only a few channels of an optimized FIR radiometer

3.1 Introduction

Since the beginning of meteorological satellites, temperature profiling has been performed with sounders in the infrared (IR) (Wark & Hilleary, 1969). The state-of-the-art instruments that probe the mid-infrared (MIR) are the Infrared Atmospheric Sounding Interferometer (IASI) (Blumstein et al., 2004), the Atmospheric Infrared Sounder (AIRS) (Aumann et al., 2003) and the Cross-track Infrared Sounder (CrIS) (Bloom, 2001). Those instruments use the 15 μm CO_2 absorption band to probe atmospheric temperature and the water vapor vibrational band at 6.3 μm to retrieve humidity profiles (Rizzi et al., 2002). This humidity profiling capability results from the strong spectral variations of the water vapor absorption in that band.

Water vapor also exhibits an extended rotational absorption band as well as a continuum in the far-infrared (FIR; 15 μm $< \lambda <$ 100 μm). This absorption band is broader than the vibrational band, hence there is more energy in this region. Previous studies have pointed out the potential of FIR for atmospheric profiling, particularly in cold regions. First, a direct consequence of the temperature dependence of the Planck function in the radiative transfer equation, emission is shifted to the FIR as the temperature of the scene decreases, offering a greater capability for cold scenes (Mlynczak et al., 2007), in contrary to the traditional 6.3 μm band quickly loses energy as the scene gets colder (Susskind et al., 2003). Practically, more than half of the radiation is lost to space in the FIR in the polar regions (Mlynczak et al., 2007). Second, the water vapor rotational absorption band in the FIR has many absorption lines with larger optical depth than the MIR, which leads to an increased sensitivity to small water vapor variations (Harries et al., 2008). The increased sensitivity is especially important in the upper troposphere,

where the water vapor concentration is scarce (Clough et al., 1992). Thus, the FIR region can be valuable for profiling the atmosphere and particularly in the stratosphere and the upper troposphere (Shahabadi & Huang, 2014).

Despite these acknowledged advantages of the FIR over the MIR for water vapor profiling, no direct spectrally resolved measurements of the atmospheric radiation have been made recently from space. The last measurements in the FIR, up to 25 μm, were made 40 years ago on two Russian *Meteor* spacecrafts and 45 years ago by the IRIS (Infrared Interferometer Spectrometer and Radiometer) instruments on the NASA Nimbus III and IV (Mlynczak et al., 2002), data that has been used to identify changes in spectral outgoing longwave radiation (Bantges et al., 2016). However at the time, the spectral and spatial resolutions of the observations, along with the large noise, prevented from getting much geophysical information out of the data. Since then, low noise liquid helium cooled bolometers operating in the far-IR have been developed, and used for instance in the Far-Infrared Spectrometer of the Troposphere (FIRST) instrument (Mlynczak et al., 2006). Such systems are however too delicate, massive and expensive to be put on a satellite. This, in combination with the intrinsic higher sensitivity of MIR sensors compared to FIR sensors, explains why no FIR satellite has been flying for decades now.

Only with the recent advent of uncooled systems operating at room temperature that have space missions in the FIR seen a renewal of interest. The series of satellite missions Climate Absolute Radiance and Refractivity Observatory (CLARREO) (Wielicki et al., 2013) is intended to measure spectrally-resolved Earth emission spectrum between 5 - 50 μm with a spectral resolution of 0.5 cm^{-1} to determine small changes in the spectral outgoing radiation (infrared and reflected solar). The mission aims at detecting decadal changes in climate forcings,

responses and feedbacks and to serve for reference intercalibration in space. It thus focuses on global or regional averages and their variations on annual timescales. As a consequence the noise-equivalent temperature difference (NETD), has the requirement to be smaller than 10 K in the FIR since averaged over a year it will be reduced to 0.01 K globally. The requirements on the absolute accuracy are on the contrary much more stringent. ESA candidate mision, called FORUM (Far Infrared Outgoing Radiation Understanding and Monitoring) (Palchetti et al., 2016) focuses on studying the forcings and the feedbacks of atmospheric water vapor and of ice clouds on the climate. The recently funded NASA PREFIRE (Polar Radiant Energy in the Far-InfraRed Experiment) CubeSat, to be launched in 2022, intends to measure in the 0-45 μm range to measure spatial and temporal variations in spectral fluxes on hourly to seasonal timescales (L'Ecuyer, 2019). (Merrelli & Turner, 2012) used the technical characteristics of CLARREO to compare two interferometers for remote sensing of temperature and humidity, with a spectral resolution of 0.5 cm^{-1}, one measuring in the MIR and another measuring in the FIR even though CLARREO was not designed to measure temperature and water vapor. They showed that there is more information content in the FIR compared to the MIR when the noise is equal in both spectral regions. However, if the uncertainty of the actual CLARREO is used for the FIR region, the advantage of the FIR is lost (Shahabadi et al., 2015).

Only a limited selection of channels among those in the water vapor absorption band of interferometers at high resolution is used in data assimilation (Fourrié & Thépaut, 2003). Supposedly, adjacent bands could thus be merged into larger bands to refine the remote sensing capability. The Arctic was selected since around 60 % of the outgoing longwave radiation is in the FIR region. Also, there is a need for precise water vapor measurements in the troposphere (Müller et al., 2016) and

especially in the Arctic (Boullot et al., 2016) and the FIR upwelling spectrum contains a large amount of potential profiling information. The objective of the present study is to design an optimal FIR radiometer to study the Arctic polar night by examining different configurations, noise levels and the trade-off between spectral resolution and noise level. Thus, this study considers a radiometer in the Arctic region using different filters or a gratings to allow different bandwiths within a spectral region. As in Observing System Simulation Experiments (OSSEs), synthetic measurements are created for different configurations of the FIR radiometer. The radiometric noise of the Far InfraRed Radiometer (FIRR) is used as a baseline to constrain the detector's performance (Libois et al., 2016b). The optimal configuration is selected with information content as a metric to lead to the best temperature and humidity analyses. The impact of FIR measurements is also evaluated in terms of their added value when assimilated on top of currently assimilated AIRS data. The experiments are done under the assumption that AIRS and the FIR radiometer are collocated and assimilated in a simple 1D assimilation system.

The paper is organized as follows. Section 2 presents the information content framework, the characteristics of the instrument, and the context of the experiments. Section 3 presents the results of the evaluation of different instrument configurations. Section 4 compares the impact of measurements of the FIR radiometer with that of AIRS measurements. A discussion and conclusions are presented in section 5.

3.2 Methods

This section first presents the characteristics of the FIR radiometer and the atmospheric conditions used in this study. Finally, we present the method used to evaluate the information content of measurements which is based on the reduction of analysis error obtained in the context of data assimilation using a numerical weather forecast as an *a priori* background state.

3.2.1 Instrument characteristics

A synthetic spaceborne FIR radiometer is considered in this study. The goal is not to investigate a particular instrument, but to explore the potential of such a novel instrument, in the framework of the preparation of the TICFIRE mission. Nevertheless, the characteristics of this radiometer are based on the FIRR instrument. The characteristics of the optics are fixed (field of view, spatial resolution, F-number, etc), only those of the detector are changed. The detector performance explore a realistic range, although the feasibility study for such performance is left to the industry. The two principal characteristics considered are its number of bands and its noise-equivalent radiance (NER). The bands are adjacent and fully cover the range of 15 - 100 μm. The transmittance is one in the bands and zero outside. The bandwidths are set in three different ways hereafter referred as 'equi-energetic', 'constant wavelength' and 'constant wavenumber'. Equi-energetic means that each band receives the same amount of energy at the top of the atmosphere (TOA), this is calculated for each atmospheric profile used. This implies that the spectral widths of the bands are not constant. Constant wavelength and constant wavenumber bands means that each bands has the same spectral width in microns or cm^{-1} respectively. The NER is varied through the experiments, but two specific NER will be highlighted, called baseline NER and target NER.

The baseline NER is equal to 0.01 $Wm^{-2}sr^{-1}$, according to the findings of (Libois et al., 2016b). Those detector characteristics are consistent with a microbolometer sensor coated with gold black for a integration time of 1 s (Proulx et al., 2009) The other specific value of NER used, target NER, is equal to 0.002 $Wm^{-2}sr^{-1}$, which is the expected NER in a few years from now, expected from efforts by the industry, mainly on the electronics and on the analog to digital conversion. Also, band splitting is achievable with a grating or filters. It was chosen to use NER instead of NETD for the radiometric resolution in order to work at the sensor level. This allows to evaluate the gain of changing the radiometric resolution and the spectral width of the bands independently. NER remains constant independently of the instrument spectral configuration, while NETD would change. Since the NER is constant, this results in less energy per band when the bandwidth is reduced. It needs to be noted the correlation between radiometric and spectral resolutions, when the number of bands increases, the signal-to-noise ratio decreases as the energy per band decreases.

Figure 3.1 shows the NETD for a blackbody at 250 K for a constant NER of 0.01 $Wm^{-2}sr^{-1}$ for an instrument with 10, 15, 20, 25 and 40 equi-energetic bands. The NETD is not constant for the bands of a configuration. This allows to compare this experiment with other studies using NETD. It shows that the NETD, for a configuration with 10 bands, is comparable to the NETD of AIRS, below 0.5 K (Garand et al., 2007), and of MODIS, less than 0.35 K (Xiong et al., 2008).

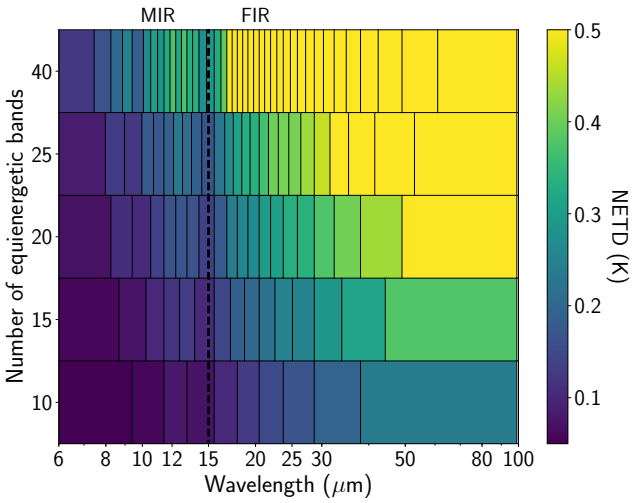

Figure 3.1 NETD for different configurations of equienergetic bands for a blackbody at 250 K with a constant NER of 0.01 $\mathrm{Wm^{-2}sr^{-1}}$. The vertical lines represent the widths of equi-energetic bands.

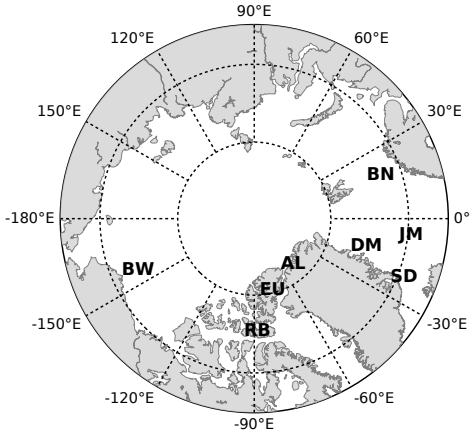

Figure 3.2 Locations of the eight Arctic stations. The letter codes are: JM- Jan Mayen; BN- Bjornoya; SD- Scoresbysunde; DM- Danmarkshavn; BW- Barrow, AL- Alert; EU- Eureka; RB- Resolute Bay.

Altitude interval (km)	Vertical resolution (km)
0 - 0.1	0.01
0.1 - 1	0.025
1 - 3	0.1
3 - 5	0.2
5 - 8	0.5
8 - 12	0.5
12 - 20	2

Tableau 3.1 Vertical resolution of the atmospheric profiles from IGRA

3.2.2 Atmospheric profiles

The radiosonde profiles are from the Integrated Global Radiosonde Archive (IGRA) database (http://www.ncdc.noaa.gov/oa/climate/igra/) (Durre et al., 2006). Figure 3.2 shows the locations of the eight stations where the different vertical profiles were taken. Those stations are the same as in (Serreze et al., 2012) and were selected to represent the various atmospheric conditions in the Arctic. It needs to be noted that the Arctic region was chosen, but those results would be similar for the Antarctic region. For each station, 6 profiles were selected randomly from the months of January or February of 2015 or 2016 in order to sample Arctic winter conditions. The profiles were truncated at 20 km altitude. Table 3.1 shows the vertical resolution of the atmospheric profiles selected. Figure 3.3 shows the averaged 48 temperature and humidity profiles selected with the red and blue lines respectively and the shaded area of the same color shows the corresponding standard deviation. The natural variability in the profiles seen through the standard deviation can be associated with different meteorological situations. The larger spread near the surface is expected since there is more variability in that region.

Also, the peak seen at 4 km in the standard deviation is due to the averaged water vapor mixing ratio being almost equal to the standard deviation at that point.

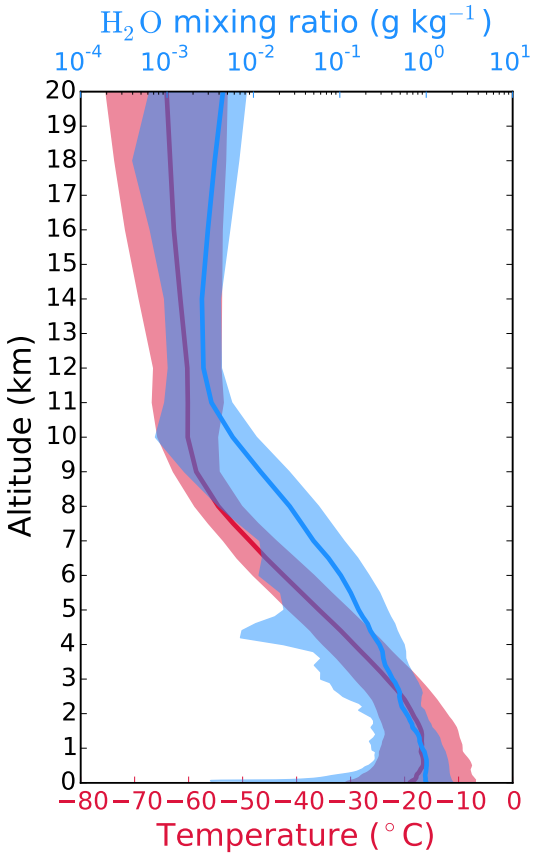

Figure 3.3 Temperature and humidity profiles averaged for the 48 radiosoundings at eight Arctic stations shown with the red and blue lines respectively. The shaded area shows the standard deviation associated with the variables.

3.2.3 Theoretical framework

In this section, the theoretical framework used is explained. This study is based on linear statistical estimation theory in the context of numerical weather prediction (NWP) (Rodgers, 2000). The different notations, definitions, approximations and data used are described in this section (Lewis et al., 2006).

The atmospheric state is represented by a vector $\mathbf{x}$ and the satellite radiance measurements at different wavelengths at the TOA are represented by the vector $\mathbf{y}$.

The observation is related to the atmospheric state through the equation

$$\mathbf{y} = H(\mathbf{x}) + \epsilon_o, \tag{3.1}$$

where H is the forward model linking the observation to the atmospheric profile and ϵ_o is the observation error. In this case, the state corresponds to atmospheric profiles of temperature, $\mathbf{T}$, and logarithm of specific humidity $\ln \mathbf{q}$ defined on k vertical levels on which the model state is defined. The dimension of the model state $\mathbf{x}$ is thus 2k. The ozone and other trace gases are kept constant. The assimilation seeks to correct an *a priori* estimate of the state of the atmosphere, $\mathbf{x_b}$, also referred to as the *background state*, using the information contained in the observations. It takes into account the relative accuracies of $\mathbf{x}$ and $\mathbf{y}$ to obtain a minimum variance estimate, $\mathbf{x_a}$, called the *analysis*.

A linearization of the forward model around the atmospheric profile, $\mathbf{x}_b$ is done, which gives, assuming that the radiative-transfer equation is weakly nonlinear near the background state

$$H(\mathbf{x}) \cong H(\mathbf{x}_b) + \mathbf{H}(\mathbf{x} - \mathbf{x}_b), \tag{3.2}$$

where $H(\mathbf{x}_b)$ is the background state in the observations space and $\mathbf{H} = \left.\frac{\partial H(x)}{\partial x}\right|_{x_b}$ is the linearized observation operator with respect to $\mathbf{x}$ evaluated at $\mathbf{x} = \mathbf{x}_b$, referred

to as the Jacobian.

The analysis, $\mathbf{x}_a$, which represent the corrected atmospheric state after the observations and the model are taken into consideration, is given by

$$\mathbf{x}_a = \mathbf{x}_b + \mathbf{K}(\mathbf{y} - \mathbf{H}\mathbf{x}_b) \tag{3.3}$$

with $\mathbf{K} = \mathbf{B}\mathbf{H}^T(\mathbf{R}+\mathbf{H}\mathbf{B}\mathbf{H}^T)^{-1}$ being the gain matrix. $\mathbf{B}$ is the background error covariance matrix and $\mathbf{R}$, the observation error covariance matrix (Rodgers, 2000). The superscript T and -1 denote respectively the transpose and inverse of a matrix.

- Jacobians

  For each band, the Jacobian indicates how temperature and humidity variations in each band impact the radiance measured at the TOA. The Jacobians were obtained by finite difference with the radiative-transfer model MODTRAN v 5.4 (Berk et al., 2005) by perturbing the background state $\mathbf{x}_b$, in this case a temperature and humidity profile. The Jacobians were computed for each band of the FIR radiometer and AIRS. A subset of 142 channels assimilated at ECCC were used for AIRS. It is assumed that the FIR radiometer and AIRS are collocated on a pixel with the same spatial response and that the lag between the instruments is negligible. More specifically, for the temperature Jacobians, $\mathbf{H}_{Ti}$, at the level i, a perturbation of $\pm$ 0.5 K was done (Garand et al., 2001). Perturbations of 1 K have been deemed sufficiently small for this experiment. This gives the variation of radiance seen at the TOA for a variation of 1 K in the atmospheric profile at each

atmospheric level. In the same manner, the humidity Jacobians in logarithm of specific humidity, s= ln q, at the level i, were obtained by perturbations of ± 0.05 q, where q is the specific humidity and $s = \ln(q)$. As shown with the following equation, in order to obtain a Jacobian with respect to a logarithm, the perturbations are done on the profile in q. Thus by multiplying the difference of perturbations by 10, this results in Jacobians with the units of $\mathrm{Wm}^{-2}\ \mathrm{sr}^{-1}\ \log(\mathrm{L}\ \mathrm{L}^{-1})^{-1}$.

$$\mathbf{H}_{s,i} = \frac{\partial R}{\partial lnq} = \frac{\partial q}{\partial lnq}\frac{\partial R}{\partial q} = q\frac{\partial R}{\partial q} \tag{3.4}$$

- Background error covariance matrix

  The matrix $\mathbf{B}$ is the background error covariance matrix associated with the background state $\mathbf{x}_b$. Figure 3.4 represents the $\mathbf{B}$ matrix used for temperature (left) and humidity (right). The $\mathbf{B}$ matrices are the stationary components of the background term of the Environment Canada assimilation system (Buehner et al., 2015). Those matrices were evaluated for a latitude of $79°\ 59'20''$, which corresponds to Eureka, Canada for the month of February. The units used are K^2 and $\log(\mathrm{L}\ \mathrm{L}^{-1})^2$ for temperature and humidity respectively. The cross-terms $\mathbf{B}_{Ts}$ and $\mathbf{B}_{sT}$ are considered equal to zero, and thus only the components $\mathbf{B}_{TT}$ and $\mathbf{B}_{ss}$ of the $\mathbf{B}$ matrix are considered. Making this approximation allows to calculate the DFS and analysis error for temperature and humidity separately. In this study, the matrices $\mathbf{B}_{TT}$ and $\mathbf{B}_{ss}$ are kept constant.

- Observation error covariance matrix

  The matrix $\mathbf{R}$ is the observation error covariance matrix. Normally, the matrix $\mathbf{R}$ takes into consideration the measurement error, the forward-model error, the representativeness error and the error associated with quality con-

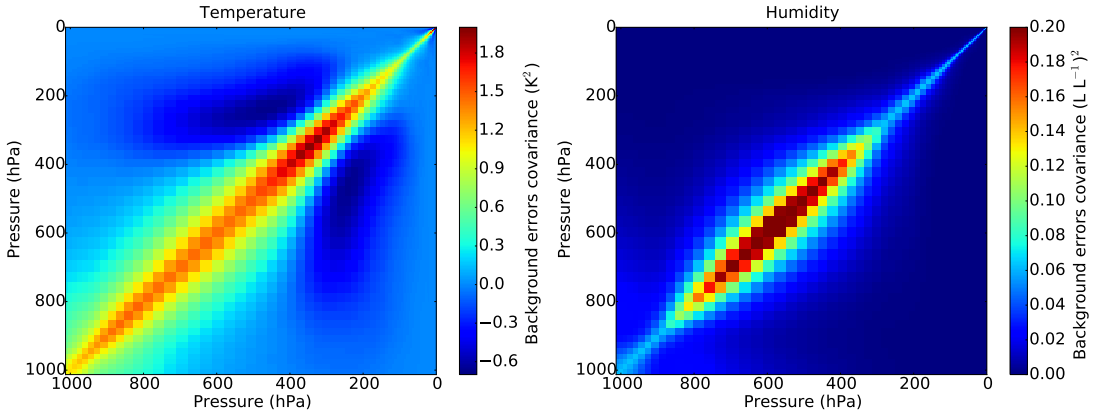

Figure 3.4 Background error covariances matrices **B** for temperature (left) and logarithm specific humidity (right) at a latitude of 79° 59′20″ for the month of February

trol to name a few (Bormann et al., 2010) but for this study, only the measurement error was considered. This approximation was taken to be consistent with previous studies in the FIR region such as (Merrelli & Turner, 2012), (Shahabadi & Huang, 2014) and (Mertens, 2002). They show that, in the thermal IR region, the main contribution to the observation error is the measurement error and also, the interchannel correlation error is small (Garand et al., 2007). The measurement error is assumed to be gaussian and unbiased, assumptions used especially in data assimilation (Rodgers, 2000). Therefore, the matrix **R** is assumed to be diagonal with the NER values on the diagonal. The spectral NER for the instrument AIRS was taken from the AIRS website (https://airs.jpl.nasa.gov/index.html) version 5 L1B data. The NER for the synthetic instrument is assumed to be constant for each configuration and each band since it comes from the sensor.

- Information content

  The impact of measurements is estimated from the analysis error covariance and the degrees of freedom per signal (DFS). The analysis error, assumed here to be unbiased, is $\varepsilon_a = \mathbf{x}_a - \mathbf{x}_t$ where $\mathbf{x}_t$ is the true state of the atmosphere. So, $\mathbf{A} = \langle \varepsilon_a \varepsilon_a^T \rangle$, with $\langle ... \rangle$ being the statistical average, is the analysis error covariance matrix and can be shown to be

$$\mathbf{A} = (\mathbf{I} - \mathbf{KH})\mathbf{B}. \tag{3.5}$$

  The reduction of analysis error due to the assimilation of observations is measured by

$$tr(\mathbf{AB}^{-1}) = N - tr(\mathbf{KH}), \tag{3.6}$$

  where $tr(\mathbf{KH}) = tr(\mathbf{HK})$. The gain in information, or the DFS is defined as

$$\text{DFS} = tr(\mathbf{HK}). \tag{3.7}$$

  The DFS can then be viewed in two ways, in the observation space and in the model space. In the observation space, the DFS measures the independent degrees of freedom measured by the observations and take into account redundancy. In the model space, it measures the reduction of analysis error with respect to the background error.

  It is an evaluation technique based on the relative errors between the observations and the prior information (Purser & Huang, 1993). It has also been

used to quantify the added value of a new set of observations by comparison with other types of measurements and also on top of measurements already assimilated (McNally et al., 2006; Lupu et al., 2011)

Thus, the analysis error variance matrix **A** and the DFS depend on the background error covariance matrix **B**, the observation error covariance matrix **R** and the Jacobian matrix **H**. The DFS will be used as a metric for obtaining the optimal configuration of the FIR radiometer and to discuss the trade-off between spectral resolution and noise level. The analysis error variance matrix will be used to see the vertical impact when the FIR radiometer is assimilated. Those calculations for the DFS and analysis error variance were done for the 48 atmospheric profiles individually, and are then averaged. The calculations for 48 atmospheric profiles show the added value on average and also its variability for the different possible atmospheric situations in the Arctic. The standard deviation spread for the DFS and the analysis error variance will be shown in figures 3.7 and 3.10 respectively.

3.3 Evaluation of configurations

3.3.1 Optimization under constraints

In this section, the DFS is used to discuss the trade-off between spectral resolution and noise level.

Figure 3.5 shows the total DFS for temperature of different configurations for a synthetic FIR radiometer with constant wavenumber configuration when the NER error level varies between 0.0003 and 0.02 $\mathrm{Wm^{-2}sr^{-1}}$ and a spectral range of 15 to 100 μm. The total number of bands varies between 1 and 200 bands. The color represents the value of the DFS for this configuration. Hence, this figure shows

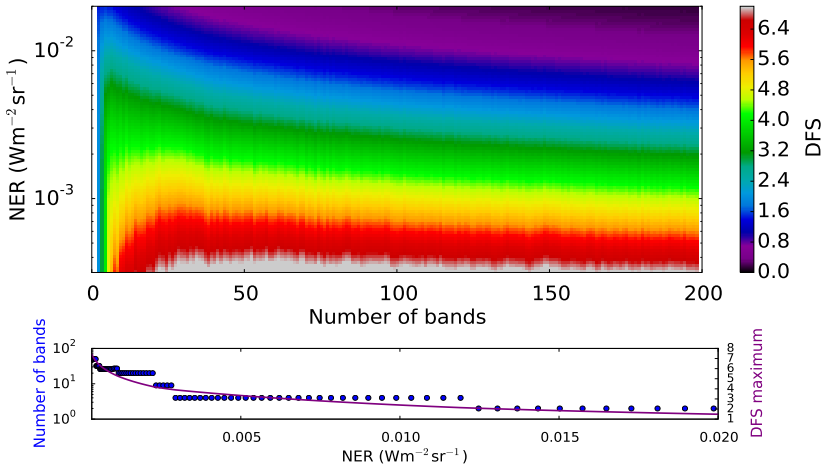

Figure 3.5 Top panel: The averaged total DFS is shown for variations of the NER level (y-axis) and variations of the total number of bands for temperature of the constant wavenumber bands configuration. The DFS for each configuration is shown with the colorbar. Bottom panel: The number of bands that maximizes DFS as a function of the NER (blue dots) and the DFS maximum as a function of the NER (purple line).

that for a fixed NER, the DFS increases and then decreases as the number of bands increases. This figure can be useful when there are technological constraints for example. If the NER is imposed by the available technology, taking a horizontal line on the top panel of figure 3.5 highlights the available spectral configurations. The maximum DFS is not with smaller bands (right side of the figure) but always with a configuration which has less than 50 bands. This is due to the constant NER. By having smaller bands, the amount of energy per band decreases and hence the signal-to-noise ratio decreases. This is also shown in the bottom panel, which shows with blue dots the number of bands of the configuration with the maximal DFS for a variation of the NER. This shows that having more bands is not always the best configuration, since the DFS is not increasing as the number of bands increases. The number of bands with the peak DFS gets larger as the NER

decreases. Another interesting way to analyze this map is by having a constraint on the number of bands an instrument can have. A radiometer can be operated with a filter-wheel and, as the number of bands increases, the rate of repetition decreases and also the cost increases.

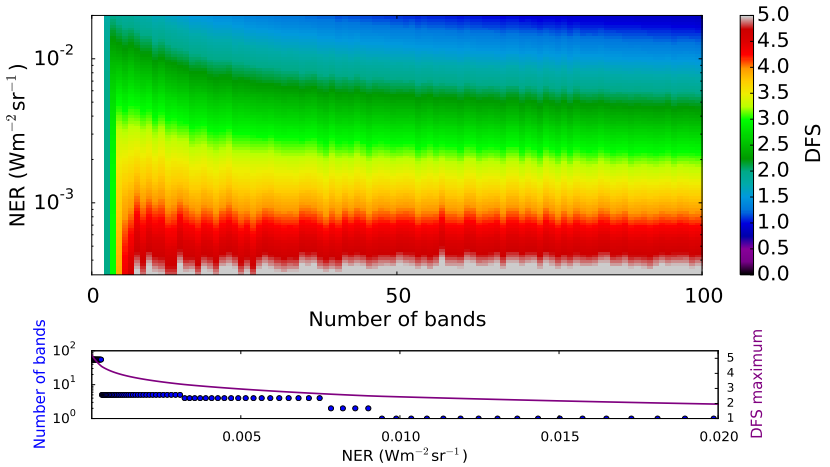

Figure 3.6 Top panel: The averaged total DFS is shown for variations of the NER level (y-axis) and variations of the total number of bands for humidity of the constant wavenumber bands. The DFS for each configuration is shown with the colorbar. Bottom panel: The number of bands that mazimizes DFS as a function of the NER (blue dots) and the DFS maximum as a function of the NER (purple line).

Figure 3.6 is similar to figure 3.5 but for humidity, but was cut off at 100 bands to better see the shift in the DFS peak. It has a lot more variability in the DFS for an horizontal line compared to temperature. This variability is partly due to spectral features of transmittance. For humidity, the maximum DFS is always obtained with a configuration which has less than 55 bands.

3.3.2 Maximisation of the total DFS

In this section, the DFS is used to find an optimal configuration for the FIR radiometer considered in this study. Three different splitting of the bands are considered, equi-energetic, constant wavelength bands and constant wavenumber bands. The instrument will be split between 1 and 250 bands.

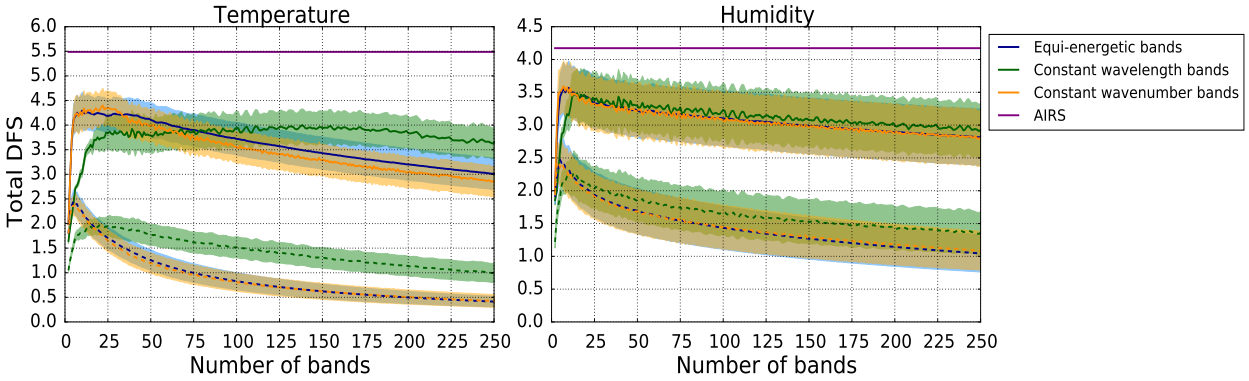

Figure 3.7 The averaged total DFS as a function of the total number of bands for three configurations which are equi-energetic bands (blue line), constant bandwidths in terms of wavelength (green line) and wavenumber (orange line) for temperature (left) and humidity (right). The dashed lines are for a NER of 0.01 $\mathrm{Wm^{-2}sr^{-1}}$ whereas the full lines are for the target NER of 0.002 $\mathrm{Wm^{-2}sr^{-1}}$. The shaded area represent the standard deviation of the 48 atmospheric profiles which are shown for all configurations except for AIRS. The standard deviation of AIRS is equal to 0.53 and 0.67 for temperature and humidity respectively. The purple line represents the averaged total DFS of AIRS for the 48 atmospheric profiles.

Considering those three configurations, figure 3.7 shows the total DFS averaged over the 48 profiles for temperature and humidity. Two values of the NER were used for the level of error, namely 0.01 $\mathrm{Wm^{-2}sr^{-1}}$ and 0.002 $\mathrm{Wm^{-2}sr^{-1}}$. To show the variability, the standard deviation is shown with the shaded area. Note that

several papers have investigated the channel selection and information content of AIRS (e.g. (Fourrié & Thépaut, 2003; Divakarla et al., 2006; Garand et al., 2007)). However, different **B** and **R** matrices were used, which prevents direct comparison with this previous work.

For temperature, for the three cases, as the number of bands increases the total DFS decreases. This is due to the constant NER, which results in less energy when the bandwidth is reduced. For the configuration having constant wavelength bands, the peak in DFS is reached with more bands compared to the other configurations. The bands being too wide near 15 μm, there is not enough resolution to capture the variation in the transmittance in this part of the spectrum. Table 3.2 shows the maximum DFS for each configuration with the corresponding number of bands for both temperature and humidity for the target noise. When the NER is reduced, there is a large increase in the DFS as expected since it means that the measurements are more accurate. For example, there is an increase by a factor of 2.00 in the DFS for the constant wavenumber band configuration when the NER goes from 0.01 $\mathrm{Wm^{-2}sr^{-1}}$ to 0.002 $\mathrm{Wm^{-2}sr^{-1}}$. For the different configurations, the standard deviation varies between 0.209 to 0.247 which is less than for AIRS which is equal to 0.513 for temperature. The highest DFS is with the constant wavenumber band configuration with 22 bands for the NER level of 0.002 $\mathrm{Wm^{-2}sr^{-1}}$. This is the configuration that will be used for temperature for the remainder of this study. The individual DFS of the optimal configuration of the 22 constant wavenumber bands is 20 % smaller than AIRS. However, when those bands are assimilated on top of AIRS, (table 3.2), the value of the DFS increases by 13.2 % compared to when AIRS is assimilated alone. This means that even after the information in the thermal IR is assimilated, there is still value in assimilating data in the FIR.

For humidity, the highest DFS is also with the constant wavenumber bands configuration with now 7 bands and a total DFS of 3.594 for the NER error of 0.002 $Wm^{-2}sr^{-1}$. For the remainder of the study, this configuration will be considered as the optimal configuration. Similarly to temperature, there is more variability for the constant wavelength configuration. For humidity, the standard deviation is larger compared to temperature, i.e. it varies between 0.318 and 0.354 depending on the configuration while it is 0.666 for AIRS. Also, when compared individually to AIRS (table 3.2), the DFS for the optimal configuration with 7 constant wavenumber bands is smaller than the DFS of AIRS by 14%. When those 7 bands in the FIR are assimilated on top of AIRS (table 3.2), the DFS increases by 11.5%, compared to assimilating only AIRS, which shows that measurements in the FIR add information when assimilated on top of AIRS data.

3.3.3 Selection of the bands with most information

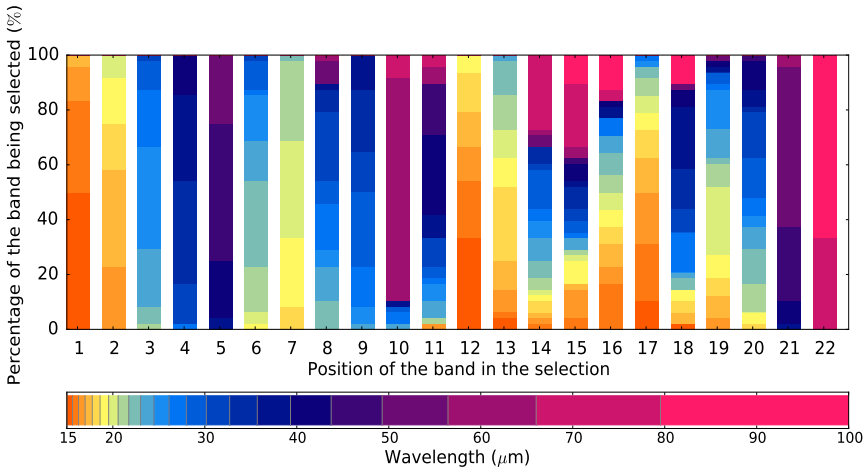

Figure 3.8 Probability of each band to be selected at each position for the 22 constant wavenumber bands with respect to temperature.

Considering a fixed number of bands for the FIR radiometer, following (Rabier

	Number of bands	DFS	Analysis error variance
	Temperature		
Constant wavenumber bands	22	4.399	12.64
Constant wavelength bands	138	3.996	-
Equi-energetic bands	10	4.294	-
AIRS	-	5.488	10.58
Background error	-	-	19.62
AIRS + constant wavenumber bands	22	6.213	9.97
	Humidity		
Constant wavenumber bands	7	3.594	1.09
Constant wavelength bands	15	3.482	-
Equi-energetic bands	10	3.569	-
AIRS	-	4.173	1.03
Background error	-	-	1.96
AIRS + constant wavenumber bands		4.714	0.95

Tableau 3.2 Total averaged DFS for a NER of 0.002 $\mathrm{Wm^{-2}sr^{-1}}$ and analysis error variance. The units for the analysis error variance is K^2 and $\log(LL^{-1})^2$ for temperature and humidity respectively

et al., 2002), we now evaluate the DFS sequentially. First, for each atmospheric profile, the DFS is calculated for each band of the configuration and the one that maximises the DFS is selected. It is shown as the first position in figure 3.8. The next band selected is the one that, when added to the previous one, adds the largest information content. This process is done until all the bands are selected. Each new band thus optimally increases the DFS. This type of calculation was also done for ice cloud properties for AIRS by (Chang et al., 2017). This selection was done for each of the 48 atmospheric profiles and for both temperature and humidity. Thus, figure 3.8 shows the frequency each band is selected at each position for the optimal configuration of the FIR radiometer with 22 constant wavenumber bands for temperature. It shows that 50 % of the time, the first band selected correspond to the first band (dark orange) in the splitting with the bandwidth 15.02-15.62 μm. In first and second position, the bands selected are always between 15.02 μm and 20.58 μm. Also, in the last position, the last band (dark pink) with bandwidth 79.53-100 μm is selected 66.67 % of the times whereas the second to last band in the splitting (bandwith 66.03-79.53 μm) is selected 33.33 % of the time.

Similarly for humidity, figure 3.9 shows the order of selection of the 7 constant wavenumber bands with respect to humidity through the atmospheric profiles. It shows that the first band selected is 58.3 % of the time the third band (mint green) which has boundaries of 19.83 - 23.62 μm whereas the second band (yellow) is selected 22.92 % of the times. For the second band selected, 62.5 % of the time, it is the 5th band (dark blue) that is selected. The last band selected is always the first band (orange) which has boundaries between 15.02 - 17.09 μm.

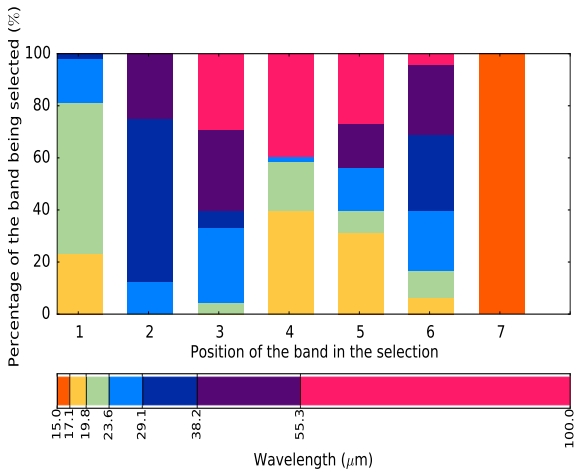

Figure 3.9 Probability of each band to be selected at each position for the 7 constant wavenumber bands with respect to humidity.

3.4 Analysis error

The impact of the observations can be seen with the analysis error variance since it provides information about the vertical distribution. The DFS previously discussed gives information integrated through the profile. Equation 4.2.1 is used to obtain the analysis error variance. To show the added value of the FIR radiometer when other types of instruments are assimilated, the instrument AIRS is considered.

Figure 3.10 shows the analysis error variance profile for temperature and humidity when the optimal FIR radiometer and AIRS are assimilated. The dark green curve represents the background error, the dark blue curve is the average over the 48 atmospheric profiles for the FIR radiometer whereas the shaded area represents the standard deviation associated with the variability obtained through the different profiles. The dark pink curve represents the averaged analysis error variance for

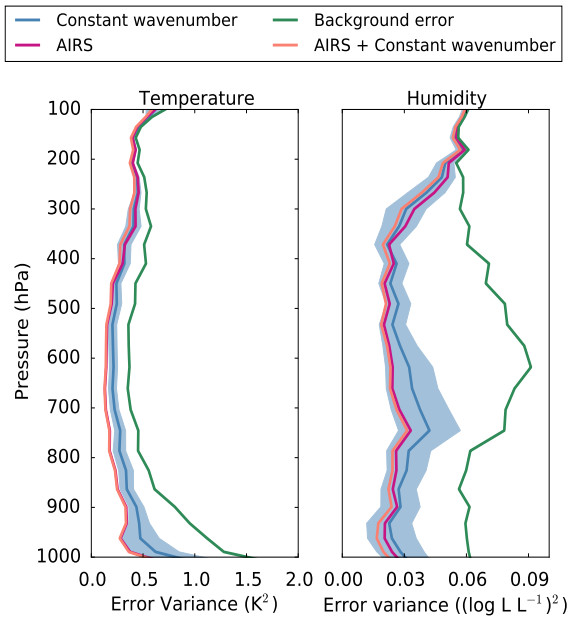

Figure 3.10 Analysis error variance profile for temperature (left) and humidity (right) for the optimized FIR radiometer. The green curve represents the background error **B**, the dark blue curve the average on the 48 atmospheric profile whereas the shaded area represents its associated standard deviation. The dark pink line is the analysis error variance of AIRS whereas the peach line represents when the optimized FIR radiometer is assimilated after AIRS.

AIRS whereas the peach curve shows when the FIR radiometer is assimilated with AIRS. For temperature, AIRS is better at reducing the error compared to the FIR radiometer except at 300 hPa. It is also at this height that the gain in assimilating the FIR radiometer on top of AIRS is seen. Also, the sum of the analysis error variance through the profile is shown in table 3.2, which allows to see the impact of the observations in the model space. Hence, assimilating the FIR radiometer after AIRS allows to reduces by 5.65 % the analysis error variance. The main gain of the FIR radiometer is with respect to humidity. The FIR radiometer is better at reducing the error in the upper atmosphere, between 400 hPa and 200 hPa,

than AIRS. When the 7 bands of the FIR radiometer are assimilated on top of AIRS, there is a non negligible gain near the surface (between the surface and 850 hPa) and in the upper part of the atmosphere (between 400 hPa and 200 hPa). The gain near the surface is due to the FIR radiometer being sensitive to the temperature inversion layer. For the different profiles, there is some variability in the atmospheric conditions which is seen with the standard deviation, especially between the surface and 600 hPa which is expected. In the same way, with table 3.2, it shows that assimilating the FIR radiometer after AIRS allows to reduce by 12.84 % the analysis error variance for humidity. (Mertens, 2002) did a similar study on the ability of the FIR to improve water vapor retrievals. The conclusions are similar in the sense that both studies find that the main reduction in the analysis error variance is between 1000 hPa and 100 hPa and that there is a gain in using both the MIR and the FIR.

To show the impact of each individual band on the analysis error variance profile, the humidity Jacobians of the FIR radiometer (left panels) and the analysis error variance associated with each of these bands when assimilated sequentially (right panels) is shown in figure 3.11 for two specific atmospheric cases with (top panel) and without (bottom panel) a temperature inversion. The colors of the bands of the Jacobians are associated with the colorbar. The top left panel of figure 3.11 shows the signature of two effects: the greenhouse effect and the presence of a temperature inversion layer. The negative peak is due to the greenhouse effect of water vapor. Increasing the humidity tends to reduce emission of radiance by masking the lower warmer layers. The positive part near the surface is due to an inversion. Increasing humidity elevates the effective emission altitude, where the atmosphere is warmer due to the inversion (Flanner et al., 2018). Moreover, as the wavelength of the band increases, the peak's height increases from around 600 hPa to 350 hPa. The top right panel of figure 3.11 shows, as in figure 3.10, the analysis

error variance for the background error, when all the bands of the FIR radiometer and AIRS are assimilated separetely which is represented by the dark green, blue and dark pink lines respectively. To show the impact on the analysis error of each band of the FIR radiometer, bands were sequentially assimilated and the analysis error variance was calculated after each new band of the FIR radiometer was assimilated. The order of assimilation of each band is the same as in section 3.3.3. It shows that the first band assimilated, the pale green one, reduces the error between 800 hPa and 300 hPa, which is where the Jacobian's peak is. The second band, navy blue one, has a higher Jacobian's peak (at around 400 hPa) and it is mainly where the analysis is reduced, between 650 hPa and 200 hPa. The next two bands assimilated, yellow and purple lines respectively, are also shown in the figure. The reduction of the analysis error near the surface is mainly due to the yellow band (17.1- 19.8 μm), which is interesting since it allows to restrain the uncertainty in the inversion layer. This illustrates the complementarity of these bands to obtain the best analysis over the whole vertical extent. Compared to AIRS (dark pink line), the FIR radiometer is better at reducing the error between 350 hPa and 250 hPa. To show the impact of the temperature inversion, the bottom panels of figure 3.11 shows the Jacobians and the analysis error variances for an atmospheric case without a temperature inversion. The left panel shows that the Jacobians are more spread out and sample the atmosphere from near the surface up to 300 hPa. Also, compared to the other case, there is no positive peak in the Jacobians which is expected since it is due to a temperature inversion layer. For the analysis error variance (bottom right panel), with the Jacobians peak being lower, the analysis error variance is less reduced compared to the case with an inversion. Even though, the FIR radiometer reduces more the analysis error variance than AIRS between 350 hPa and 200 hPa. Also, near the surface, the FIR radiometer is better at reducing the analysis error variance when there is an inversion.

3.5 Conclusions

The objective of the present study is to design an optimal FIR radiometer to study the Arctic polar night by examining different configurations, noise levels and the trade-off between spectral resolution and noise level. This was investigated through an information content analysis based on optimal estimation method. The optimal configuration for the synthetic FIR radiometer is with 22 constant wavenumber bands for temperature and 7 constant wavenumber bands for humidity. It was shown that too many bands with a large noise do not give enough information on the atmosphere. With a few bands, it was possible to get a DFS similar to AIRS when compared individually. Given that AIRS provides information also on both temperature and humidity, the impact of assimilating FIR measurements on top of AIRS data was evaluated by the reduction in analysis error variance. With respect to temperature, there is a small impact in assimilating the FIR radiometer measurements over AIRS between 400 and 250 hPa. On the contrary, for humidity, there is a non negligible gain near the surface (between the surface and 850 hPa) and in the upper part of the atmosphere (between 400 hPa and 200 hPa). Something else that is worth noting is that between 400 hPa and 200 hPa, taken individually, the FIR radiometer is better at reducing the humidity analysis error variance than AIRS.

Measurements in the FIR are unlikely to be assimilated in the next few years in NWP systems, however the results shown in this paper highlight the potential of this new type of observations which may become available in the next decade. It is non negligible to get results similar to AIRS in reducing the analysis error for humidity with only 7 bands compared to a subset of 142 bands from AIRS. FIR measurements could be used in regions where there is still large uncertainties in

water vapor retrieval or assimilation. It was shown to be useful for retrieval of water vapor in the 400 hPa to 200 hPa region for the Arctic, but FIR radiometry can be useful in other regions as well.

The results presented here, are based on a 1D assimilation of two collocated instruments. Another interesting aspect of this study is the method, which facillitates testing rapidly multiple configurations of an instrument. Also, it allowed to compare the relative impact of measurements in the FIR and the MIR. However, there are limitations to this approach that need to be kept in mind. Because a satellite does provides measurements over the whole globe, it would be important to examine the impact one could expect in other regions such as the Tropics for instance. Finally, complex Observing Simulated Systems Experiments (OSSEs) would be needed to evaluate the global impact in a context including all observations currently assimilated.

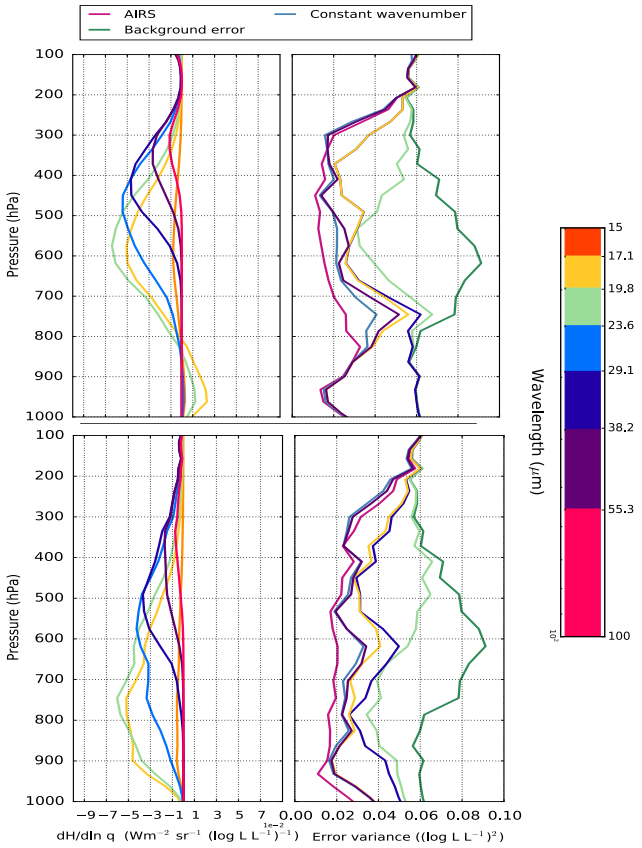

Figure 3.11 Left panels show the humidity Jacobians for the FIR radiometer associated with two atmospheric cases, which are with (top panel) and without (bottom panel) a temperature inversion. The different colors are the 7 associated bands of this configuration shown by the colorbar which is valid for both panels. The right panel show the analysis error variance for the two cases. The curves from right to left are the background error, when the bands of the FIR radiometer are assimilated one at the time from one band to four (light green, dark navy, yellow and purple), when all the 7 bands are assimilated and AIRS is assimilated.

CHAPITRE IV

A COMPARISON OF CHANNEL SELECTION FOR THE ASSIMILATION OF CRIS RADIANCES FOR NWP

Ce chapitre présente un article en préparation

Coursol, L., Heilliette S., Gauthier, P (2023). A comparison of channel selection for the assimilation of CrIS radiances for NWP. En préparation

Une sélection de canaux optimale pour l'instrument CrIS a été trouvée à l'aide du contenu en information. Cette sélection de bandes a été comparée à des sous-ensemble de canaux faites pour d'autres centres de prévision numérique du temps. La sélection de canaux de Carminati (2022) a 224 canaux identiques à la configuration optimale, mais en termes d'erreur d'analyse les deux ensembles de canaux sont très semblables. Différentes matrices de covariances d'erreur d'observation ont été considérées afin d'évaluer l'impact de cette matrice sur la sélection de canaux. Même si les canaux sélectionnés optimalement sont différents dépendant des différentes matrices $\mathbf{R}$, les résultats en termes d'erreur d'analyse sont similaires.

A comparison of channel selection for the assimilation of CrIS radiances for NWP

Laurence Coursol[1], Sylvain Heilliette[2] and Pierre Gauthier [1]

[1] Université du Québec à Montréal (UQAM), Montréal, Canada

[2]Data Assimilation and Satellite Meteorology Research Section, Environment Canada, Dorval, Quebec, Canada

[1] Corresponding author: Laurence Coursol, laurence.coursol@gmail.com

Abstract

With hyperspectral instruments measuring radiation emitted by the earth and its atmosphere in the thermal infrared range in multiple channels, several studies were made to select a subset of channels in order to reduce the number of channels to be used in a data assimilation system. An optimal selection of channels based on information content depends on several factors related to observation and background error statistics and the assimilation system itself. An optimal channel selection for CrIS was obtained and then compared to selections made for different NWP systems. For instance, the channel selection of (Carminati, 2022) has 224 channels identical to our optimal selection which includes 455 channels. However, in terms of analysis error variance, the difference between the two selections is small. Integrated over the whole profile, the difference is equal to 7.4 K^2 and 0.077 $(logLL^{-1})^2$ for temperature and humidity respectively. Also, different observation error covariance matrices were considered to evaluate the impact of this matrix on channel selection. Even though the channels selected optimally were different in terms of which channels were selected for the various $\mathbf{R}$ matrices, the results in terms of analysis error are similar.

4.1 Introduction

Previous generations of thermal infrared vertical sounders such as HIRS provided measurements over a few spectral bands referred to as channels. From those measurements, it was possible to retrieve atmospheric vertical profiles of temperature and humidity with a coarse vertical resolution, since at those wavelengths the radiance varies with temperature, humidity and other constituents. This small number of channels per measurement made it possible to assimilate most of the channels in NWP centers (Prunet et al., 1998). With the advancement of hyperspectral instruments on satellites containing thousands of sounding channels in the thermal infrared ($3.7\mu m < \lambda < 15\mu m$), research aimed at finding an optimal subset of channels that would provide most of the information available from the measurements started. (Rodgers, 1998) did a case study to explore the use of information content (or degrees of freedom, DFS) to optimize the channel selection of a spectrometer for remote sounding. The instrument AIRS with 2378 channels measuring in the thermal infrared was used (Aumann et al., 2003) and they found that most of the information content on atmospheric temperature and humidity could be retrieved from a subset of up to 1000 channels.

Several studies were done on channel selection for the instruments AIRS, IASI and CrIS (Cross-track Infrared Sounder). (Rabier et al., 2002) tested different methods to obtain an optimal subset of channels in an operational NWP context for the instrument IASI, including the iterative DFS and the Jacobian method, which is based on the characteristics of the Jacobians. They concluded that an iterative method using the DFS gives better results at reducing the analysis error than the Jacobian method, but it is more expensive in computational time. Similarly, (Fourrié & Thépaut, 2003) compared the operational channel selection with

the iterative DFS method introduced by (Rabier et al., 2002) for the instrument AIRS. They concluded that the iterative DFS method was slightly better and the channels selected were different, but gave similar results in terms of analysis error for temperature, humidity and ozone. (Gambacorta & Barnet, 2012) also did a channel selection for CrIS based on the Jacobians and their physical properties. A subset of 399 channels was selected, representing the full atmospheric variability contained in the original spectrum. However, the goal of channel selection is to find a selection of channels that most reduce the uncertainty in the analysis and not to represent the full atmospheric variability. (Carminati, 2022) compared the previous selection with one based on the iterative DFS. There is a large variability in the channels selected by the two methods with only one third being identical. Still, the selection made with the DFS gave better results in improving most of the forecasts. This shows that there are still a lot of issues to be explored regarding the channel selection of an instrument since it is dependent on the method used and also the assumptions made. For example, the impact of correlations of the observation error covariance matrix (Coopmann et al., 2020) on channel selection and the variation of the selection with respect to seasons and regions (Fourrié & Thépaut, 2003) have been examined previously.

The goal of this paper is to find a subset of physical channels optimal for the instrument CrIS with the DFS method similarly to (Carminati, 2022) but with a different observation error covariance matrix and a different set of atmospheric profiles. Comparison of channel selections have not been previously done in other studies. The channel selection methodology is explained in section 2. The results of the channel selection are discussed in section 3. The selection will be compared to the one based on Jacobians used at Environment and Climate Change Canada (ECCC) and the one from (Carminati, 2022) in section 4. This will be followed

by a discussion on the impact of the observation error covariance matrix on the selection in section 5. Conclusions are drawn in section 6.

4.2 Methods

4.2.1 Theoretical framework

This study is based on linear statistical estimation theory in the context of NWP (Rodgers, 2000). The different notations, definitions, approximations and data used are described in this section. The general framework presented in (Coursol et al., 2020) is followed.

The atmospheric profiles of temperature, $\mathbf{T}$, logarithm of specific humidity $s = \ln \mathbf{q}$ and surface temperature at a given location define the state vector represented by the vector $\mathbf{x}$. The observations, represented by a vector $\mathbf{y}$, are satellite radiance measurements chosen at nadir at different wavelengths taken at the TOA. The satellite observation is related to the atmospheric state through the equation

$$\mathbf{y} = H(\mathbf{x}) + \epsilon_O + \epsilon_F, \tag{4.1}$$

where H is an observation operator including the radiative-transfer model while ϵ_o is the measurement error with the associated error covariance matrix $\mathbf{O}$. The observation error covariance $\mathbf{R} = \mathbf{O} + \mathbf{F}$ includes the measurement error covariance matrix but also the forward-model errors covariance $\mathbf{F}$.

Ozone and other trace gases are kept constant to climatological values whereas the assumption was made that the surface temperature is equal to the first atmo-

spheric temperature level near the surface. A linearization of the forward model is done around the background state $\mathbf{x}_b$, which gives

$$H(\mathbf{x}) \cong H(\mathbf{x}_b) + \mathbf{H}(\mathbf{x} - \mathbf{x}_b), \tag{4.2}$$

assuming that the radiative-transfer equation to be weakly nonlinear near the background state.

In the last equation, $H(\mathbf{x}_b)$ is the background state in the observation space and $\mathbf{H} = \frac{\partial H(x)}{\partial x}\Big|_{x_b}$ is the linearized observation operator with respect to $\mathbf{x}$ evaluated at $\mathbf{x} = \mathbf{x}_b$, referred to as the Jacobian. Jacobians are used to evaluate changes in radiances associated with a perturbation of the background state. Assuming also the background error covariance matrix $\mathbf{B}$ is known, the analysis, $\mathbf{x}_a$ can be obtained as

$$\mathbf{x}_a = \mathbf{x}_b + \mathbf{K}(\mathbf{y} - \mathbf{H}\mathbf{x}_b) \tag{4.3}$$

with $\mathbf{K} = \mathbf{B}\mathbf{H}^T(\mathbf{R}+\mathbf{H}\mathbf{B}\mathbf{H}^T)^{-1}$ being the gain matrix, which minimizes the total analysis error variance (Rodgers, 2000). The superscript T and -1 denote the transpose and inverse of a matrix respectively.

4.2.2 Atmospheric profiles and Jacobians

Radiosonde profiles were obtained from the Integrated Global Radiosonde Archive (IGRA) database (http://www.ncdc.noaa.gov/oa/climate/igra/) (Durre et al., 2006). Ten stations were selected to cover different regions and seasons and to

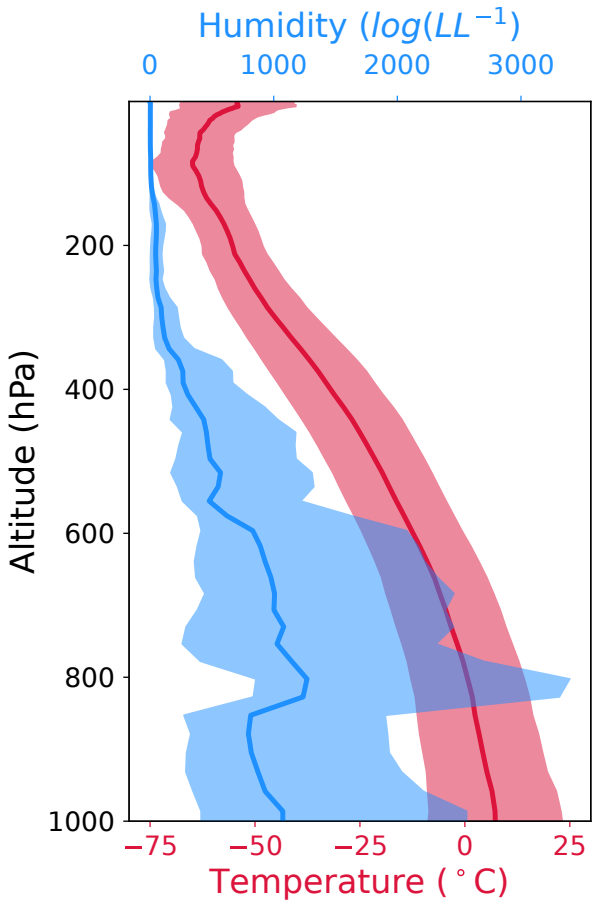

Figure 4.1 Temperature and humidity profiles averaged for the 50 atmospheric cases shown with the red and blue lines respectively. The shaded area shows the standard deviation associated with the variables.

have some atmospheric variability. Figure 4.2 shows the location of the selected radiosonde profiles. For each station, 5 profiles were randomly selected between the years 2015 and 2019 for a total of 50 profiles. Figure 4.1 shows the averaged 50 temperature and humidity profiles selected with the red and blue lines respectively and the shaded area of the same color shows the corresponding standard deviation. The profiles were interpolated to the RTTOV v.12 (Saunders et al., 2018) 101 pressure levels. The maximum and minimum pressures are 1100 and

0.005 hPa. For levels higher than 70 hPa, an extrapolation was done for humidity. It was replaced by the value of the humidity at 70 hPa multiplied by the ratio of the pressure at that level over 70 hPa cubed.

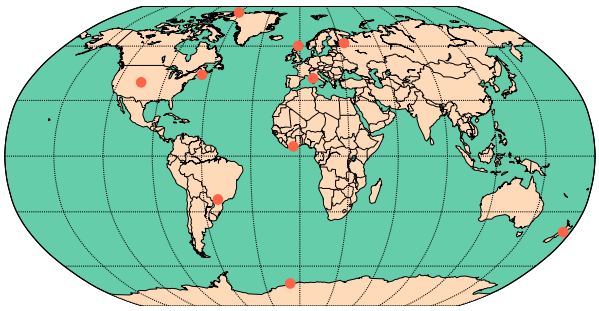

Figure 4.2 Locations of the stations selected

For each channel, the Jacobian indicates how temperature and humidity variations at each wavelength impact the radiance measured at the TOA. The Jacobians were obtained from RTTOV model, RTTOV v.12, a fast radiative transfer model for data assimilation and retrieval systems for each profile provided by the background state. The Jacobians were computed for each channel of CrIS, for a total of 2211 channels. In order to avoid selecting bands sensitive to unwanted gases and spectral regions, certain bands were eliminated. In this case, bands sensitive to ozone, methane and CO, and also bands too sensitive at the TOA were excluded similarly to (Collard, 2007). After this step, there were 1614 channels that remain available.

4.2.3 Error covariances matrices

The **R** matrix normally includes the measurement error, the forward-model error, the representativeness error and the error associated with quality control and other sources (Bormann et al., 2010). For this study, only the measurement error

was considered for the experiment with the central field of view (number 5) taken since it has the best characteristics and is the one received at NWP centers (Denis A. Tremblay, personal communication). This approximation was taken since it is a theoretical experiment and the specific details of the composition of the observation error covariance matrix have less importance. Also, this approximation was taken in order to be consistent with our previous paper (Coursol et al., 2020) and with previous studies such as (Merrelli & Turner, 2012), (Shahabadi & Huang, 2014) and (Mertens, 2002). (Noh et al., 2017) also gave an explanation to why considering the measurement error is sufficient for this type of experiment since theoretically-generated observations and background data are independent of the scale mismatch between the observation and model.

Radiances are assumed to be apodised, which introduces some correlations between adjacent channels. The measurement error is assumed to be Gaussian and unbiased, which are assumptions used especially in data assimilation (Rodgers, 2000). Nevertheless, the matrix $\mathbf{R}$ is taken to be diagonal with the noise-equivalent radiance (NER) values on the diagonal. In the section 5 related to the sensitivity to the $\mathbf{R}$ matrix, a complete observation error covariance matrix from ECCC will be used. Also, a $\mathbf{R}$ matrix composed of the measurement error and a forward-model error of 0.2 K in radiance space with a radiance spectrum associated with the scene as in (Fourrié & Thépaut, 2003) and (Rabier et al., 2002) will be used.

We took the stationary version of the $\mathbf{B}$ matrix for temperature and humidity that has been used in the ECCC assimilation system (Buehner et al., 2015). Those matrices were evaluated at the locations of the radiosondes profiles used and averaged over the whole year. The units used are K^2 and $\log(L\ L^{-1})^2$, where $L\ L^{-1}$ represents the ratio of volume of water vapor over the volume of air, for tem-

perature and humidity respectively. For the time being the surface temperature has not been included in the control variables. The cross-terms of the **B** matrix between temperature and humidity are neglected. In this study, the **B** matrices for temperature and humidity are kept constant in time at each station, but differ from one station to another.

4.2.4 Information content

To quantify the gain in information brought by measurements, the analysis error covariance and information content are needed. The analysis error, assumed here to be unbiased, is $\varepsilon_a = \mathbf{x}_a - \mathbf{x}_t$ where $\mathbf{x}_t$ is the true state of the atmosphere. So, $\mathbf{A} = \langle \varepsilon_a \varepsilon_a^T \rangle$, with $\langle ... \rangle$ being the statistical average. At optimality, the best linear unbiased estimate is obtained and it can be shown that (Rodgers, 1998)

$$\mathbf{A} = (\mathbf{I} - \mathbf{KH})\mathbf{B}. \tag{4.4}$$

The reduction of analysis error due to the assimilation of observations is measured by

$$tr(\mathbf{AB}^{-1}) = N - tr(\mathbf{KH}), \tag{4.5}$$

where $tr(\mathbf{KH}) = tr(\mathbf{HK})$, tr defined as the trace of a matrix and N is the number of pressure levels. The gain in information is defined as

$$\text{DFS} = tr(\mathbf{HK}). \tag{4.6}$$

where DFS stands for degrees of freedom per signal. It gives a measure of the

reduction of uncertainty brought in by the analysis based on the relative errors between the observations and the prior information (Purser & Huang, 1993) and only depends on the background error covariance matrix **B**, the observation error covariance matrix **R** and the Jacobian matrix **H**. The DFS will be computed for subsets of channels and used to find an optimal selection that provides the most information for CrIS.

With the background and observation error covariance matrices defined, it is possible to calculate the DFS for temperature and humidity for the 50 atmospheric profiles for all channels sequentially. For each profile, the DFS for each channel of CrIS is calculated and the channel with the largest DFS is selected. The DFS is calculated again for the channel selected in combination to one of the remaining channels not selected previously. The combination of channels which yields the largest DFS is then taken. This calculation is done until 400 channels are selected. The cut-off of 400 channels was selected to reduce the calculation time and since the information content becomes saturated at this limit as can be seen in figure 4.3. This cut-off conforms with the one chosen in (Carminati, 2022) and (Coopmann et al., 2020).

Figure 4.3 shows the averaged DFS over the 50 atmospheric profiles for temperature and humidity as a function of the number of channels selected up to 400. The DFS grows rapidly as the first few channels are selected since most of the information required for improving the background state is contained in those first few. The DFS for temperature increases more rapidly compared to humidity for the first 40 channels and afterwards the growth rate is similar. At 400 channels, the DFS for both temperature and humidity is close to the total averaged DFS (dashed lines) obtained when assimilating all channels. The values of the DFS at 400 channels are 11.4 and 8.0 for temperature and humidity respectively. At 400 channels, over 97% of the total information is contained out of the total av-

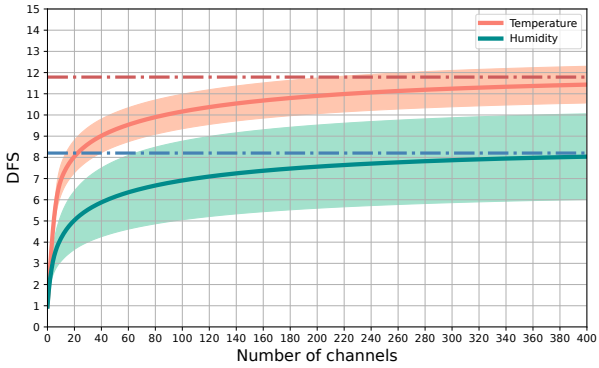

Figure 4.3 Averaged DFS over the 50 profiles for temperature (orange) and humidity (blue) (full lines) whereas the dotted lines show the associated total DFS for the respective variable. The shaded area shows the standard deviation associated with the variables.

eraged DFS for both temperature and humidity. The shaded area in figure 4.3 show the variability from the different atmospheric conditions from the set of 50 atmospheric profiles. As expected, the standard deviation is bigger for humidity than temperature.

Another way to view these results is through the analysis error variance, since the information gained from the addition of channels translates as error reduction. Figure 4.4 shows the analysis error variance for both temperature and humidity for different configurations. With respect to temperature, CrIS significantly reduces the analysis error variance, up to 27.3 % of the background error when 100 channels are considered (orange curve) and 29.7 % when 400 channels are assimilated optimally (blue curve). Even though the surface temperature is not considered, selected Jacobians peaking close to the surface results in a large reduction in analysis error variance close to the surface. Also, the shaded area shows the variability of the results amongst the 50 profiles. Among the profiles, there is

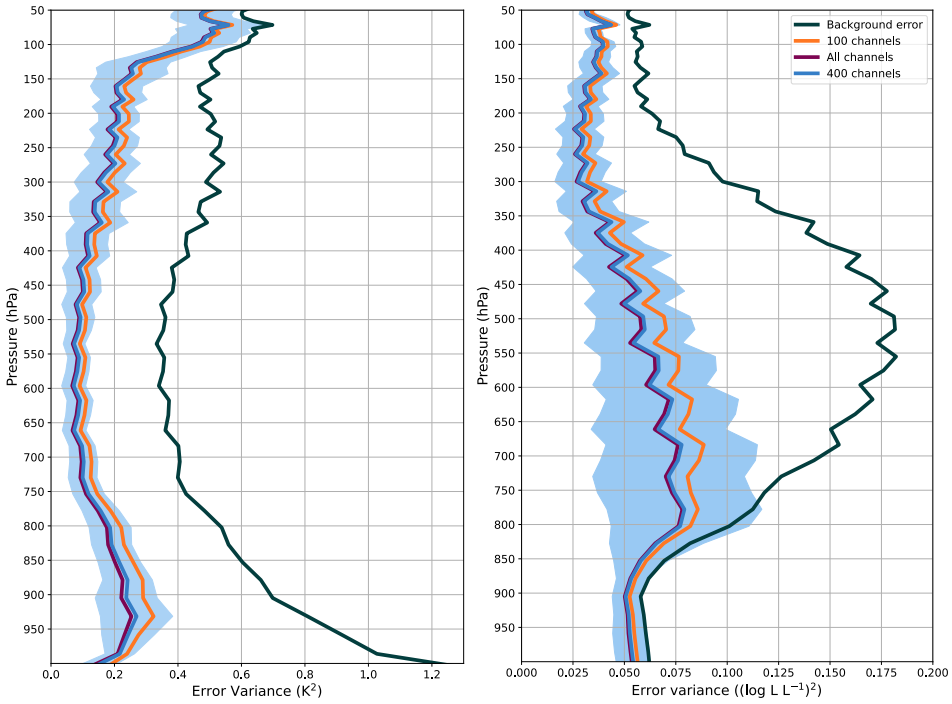

Figure 4.4 Analysis error variance profile averaged over the 50 atmospheric profiles for temperature (left) and humidity (right). The black curve represent the background error **B**, the orange curve represent when 100 channels are taken optimally, the blue curve when 400 channels are selected optimally, whereas the shaded area represents its associated standard deviation and the dark purple curve when all the channels are assimilated.

cases from summer and winter which can have a large variability for regions such as the mid-latitudes. This shows the impact of the observations on the analysis varies with the atmospheric conditions. It can also be seen that the difference between 400 channels (blue curve) and all the channels (dark purple curve) is small, and that the largest difference is near the surface. For humidity, the bulk of the analysis error reduction is between 800 and 200 hPa where the background error variance is the largest (black curve), i.e. 41.6 % when 100 channels are consid-

ered (orange curve) and 46.2 % when 400 channels are assimilated optimally. The larger variability with respect to reducing the analysis error variance is between 800 and 400 hPa which corresponds to a region with large variability in humidity. Similarly to temperature, the difference in analysis error between 400 channels and all the channels is minimal.

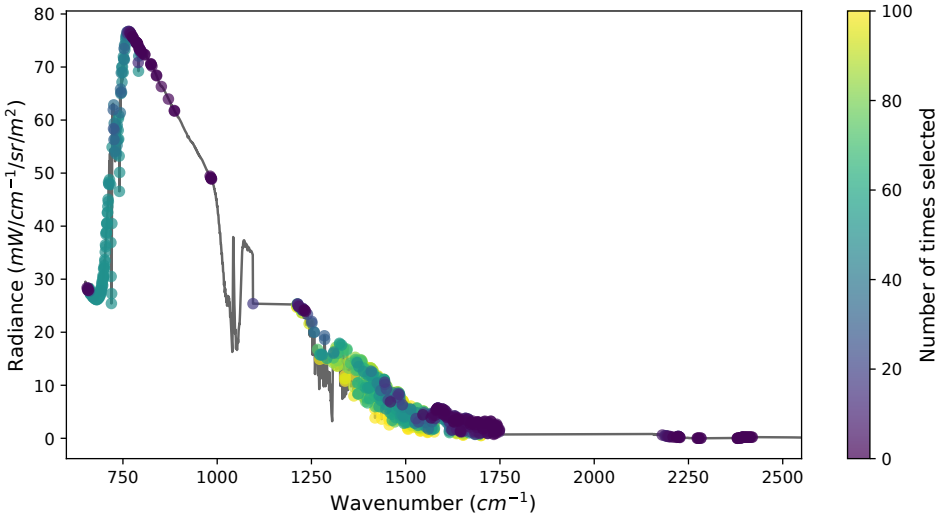

Figure 4.5 Frequency of selection of the different channels out of 100 (50 for temperature and 50 for humidity) shown by the color superposed with a spectral radiance as a function of the wavenumber

To find an optimal selection of channels for CrIS and to analyse more specifically the selection process, figure 4.5 illustrates the number of times a band is selected out of the 50 atmospheric cases for both temperature and humidity taken together (hence out of 100) at the wavenumber associated with this channel. Separately, for the 50 atmospheric profiles, 149 and 200 channels are always selected for temperature and humidity respectively. If taken together for temperature and humidity as in figure 4.5, it represents 40 different channels that are always selected. On the other hand, there are 858 and 1030 out of 1614 available channels that are never

selected for temperature and humidity respectively. There are then 738 channels that are never selected when considered together. Figure 4.5 shows as expected that channels are selected in the 650-770 cm^{-1} band which is normally used for temperature sounding. Similarly, many channels are selected in the 1210-1750 cm^{-1} band which is used for sounding humidity. Moreover, no channel is selected in the ozone band (1000-1070 cm^{-1}) since the channel selection was not optimized with respect to that variable. The channels selected at least once as shown in figure 4.5 can be sorted according to their selection frequency. Therefore, the 400 most frequently selected channels will become the optimal selection of channels for both temperature and humidity. This method of taking the most frequently selected channels was compared in (Coopmann et al., 2022) to a selection made by taking the first rank selected channels and showed that for a larger number of channels selected the first method yields better results with respect to information content. The averaged DFS for both the most frequently selected channels and the first rank selected channels were calculated and the same conclusions as in (Coopmann et al., 2022) were obtained. In our case, if we stop at exactly 400 channels, there are still channels left out that have the same frequency of selection and since they have the same frequency, they were added so that 455 channels were retained for the optimal selection. Those channels selected for the rest of the experiment, shown in figure 4.6, will represent the optimal selection of channels for CrIS.

4.3 Comparison with other selections of CrIS

Since the selection is dependent on the observation error covariance matrix $\mathbf{R}$ and the background error covariance matrix $\mathbf{B}$, the selection of channels can change for different NWP systems. In this section, the previous optimal selection will be compared with two selections for CrIS previously done, one from ECCC and one

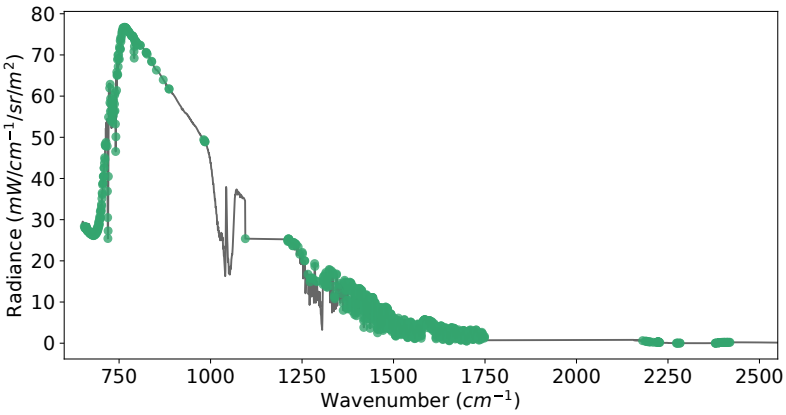

Figure 4.6 Position of the channels selected for the optimal selection of 455 channels superposed with a spectral radiance as a function of wavenumber

from (Carminati, 2022).

4.3.1 ECCC selection

To compare the selection of ECCC composed of 103 channels selected with the Jacobians method, a subset of channels of the selection done in this paper was considered. In order to have around the same number of channels as the selection of ECCC, a subset of 104 channels were considered optimally selected. 104 channels were selected instead of 103 for the same reason as previously explained, since channels had the same frequency of selection.

To show the added-value of the different selections, figure 4.7 shows the analysis error variance for different selections for both temperature and humidity. The dark blue curve represents the averaged analysis error when the selection of 103 channels of ECCC is considered whereas the light blue curve represents the av-

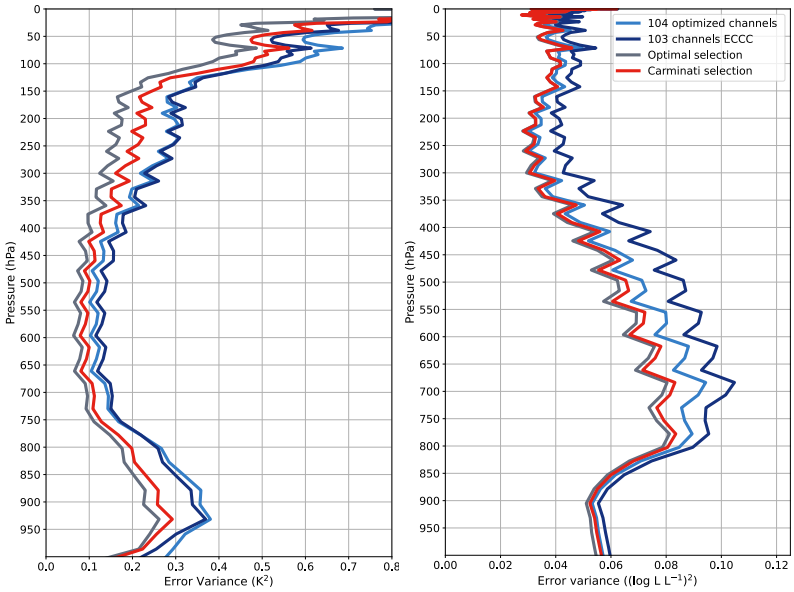

Figure 4.7 Profiles of analysis error variance for different selections for temperature (left) and humidity (right). The different selections are 104 optimal channels (light blue), 103 channels from ECCC (dark blue), selection from (Carminati, 2022) (431 channels) (red) and the optimal selection of 455 channels (gray).

eraged analysis error when 104 channels are selected optimally. For temperature, the selection of 103 channels of ECCC reduces more the error compared to the optimal selection of 104 channels whereas it is the inverse for humidity.

Integrated through the whole profile, the difference in reducing the analysis error is equal to 4.5 K^2 and -0.63 $(logLL^{-1})^2$ for temperature and humidity respectively between the optimal selection of 104 channels and the ECCC one. Those non-optimal results for a selection of 103 channels is expected since as shown in figure 4.3, a selection of 103 channels doesn't contain most of the information available as the curve for the averaged DFS for temperature and humidity is still increasing as more channels are selected. The 103 channels selected by ECCC contain only 69.7 % and 49.1% of the total information available with respect to temperature

Tableau 4.1 Averaged DFS and the reduction in error compared to the background error covariance over the 50 atmospheric profiles for the optimal selection and the Carminati selection

	Analysis error reduction (%)		DFS	
	Temperature	Humidity	Temperature	Humidity
Optimal selection	46.1	45.6	14.5	7.3
Carminati selection	38.8	43.3	12.2	7.2

and humidity respectively when the DFS are compared. 6 channels are identical between the selection of ECCC and the optimal selection of 104 channels.

4.3.2 Carminati et al. selection

Similarly, the optimal selection from this experiment can be compared to the selection made by (Carminati, 2022). The biggest differences between the selections from the Carminati experiment is the observation error covariance matrix $\mathbf{R}$, estimated with the method of (Desroziers et al., 2005). Also, the DFS was calculated for ozone and surface temperature which are not considered in our study. The optimal selection of (Carminati, 2022) retains 431 channels to match the number of channels previously selected in other studies such as in (Gambacorta & Barnet, 2012) shown in figure 4.8 with the red points. Hence, the optimal selection of 455 channels is compared to the selection of (Carminati, 2022). Figure 4.7 shows also the analysis error variance corresponding to the assimilation the channels selected by (Carminati, 2022) (red) and an optimal selection of 455 channels (gray). These were averaged over the 50 atmospheric cases.

For temperature, the optimal selection is better at reducing the analysis error

compared to the Carminati selection. The largest differences are between the surface and 800 hPa, which is expected since it is where there is the largest variability with respect to temperature. For humidity, both selections give almost identical results as can be seen in table 4.1. The difference in the reduction of the analysis error between the two selections could be explained by the different atmospheric profiles selected for the different experiments. (Carminati, 2022) used one profile for each region for a total of 40 cases whereas in our study 5 profiles per region were considered in order to account for the atmospheric variability possible in different regions. Also, the Carminati selection and the optimal selection share 224 identical channels out of the 455 contained in the optimal selection shown in figure 4.8 with the yellow points. Most of two channels are in the temperature and water vapor bands. One of the differences is due to ozone being considered as one of the variables for the channel selection of Carminati. This shows that even if channel selections for an instrument is different, the final impact on analysis variance is similar.

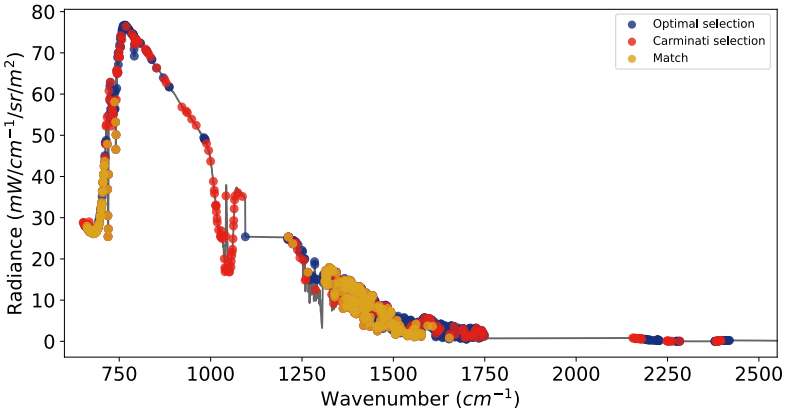

Figure 4.8 Position of the channels selected for the optimal selection of 455 channels (blue), for the Carminati selection (red) and the channels that match for both selections (yellow) superposed with a spectral radiance as a function of wavenumber

4.4 Impact of the observation covariance error matrix

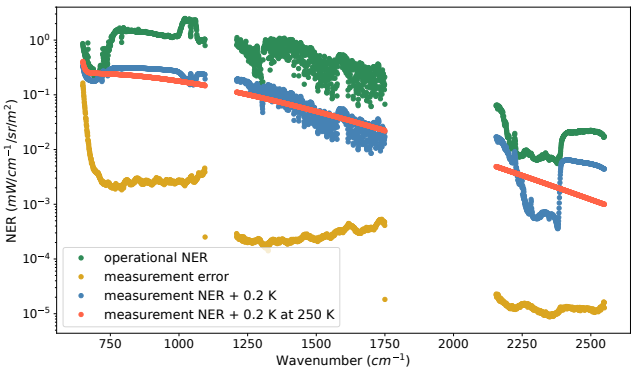

Figure 4.9 Variance of different observation covariance error matrices. The yellow curve represents the measurement error, whereas the green curve represents the variance of the operational observation error covariance matrix used at ECCC. The orange and blue curves represent the sum of the measurement error variance and two forward error, one constant evaluated at 250 K and one variable evaluated at the temperature scene respectively.

The previous section showed that various experiments configurations from NWP centers can lead to different results with respect to CrIS selection of optimal channels. For instance, the channel selection depends on the observation error covariance used. This section examines the sensitivity of the selection to this particular aspect for one region in the mid-latitudes. Figure 4.9 shows the variance associated with different observation error covariance matrices $\mathbf{R}$ used as a function of the wavelength. The yellow curve represents the measurement error that was considered for the main part of our study whereas two other types of observation error covariance matrices were considered. The green curve represents the operational observation error covariance matrix used at ECCC for the data assimilation system. Another observation error covariance matrix normally

used for channel selection of an instrument is to take the measurement error and to add a constant error of 0.2 K to consider the radiative-transfer-model error (Fourrié & Thépaut, 2003), called the forward error. However, those infrared instruments measures radiance in $mW/cm^{-1}/sr/m^2$ and not in brightness temperature. Hence, to convert those, a constant brightness temperature of 250 K is considered and not the temperature of the scene which is dependent on the wavelength. An error is introduced with this assumption. To illustrate this, to the measurement error, two forward error are added separately, both of 0.2 K but one at 250 K (orange curve) and one evaluated at the brightness temperature of the scene (blue curve).

Also, the analysis error variance for both temperature and humidity behave as expected: larger observation error variances matrix leads to larger analysis error variance (not shown). Thus, in order of less reduction to most reduction, there is the operational observation error covariance matrix, the measurement error with the constant forward error and then the measurement error with the variable forward error. However, even though the operational observation error is one order of magnitude bigger than the measurement error with a forward error, the analysis error reduction is comparable. The percentage of difference between the total analysis error variance for the operational observation error and the measurement error with a forward error (orange and blue curves) is around 10.3 % for temperature and 8.3 % for humidity.

To compare the impact of the observation error covariance matrices on the channel selection, for each different $\mathbf{R}$ matrix shown in figure 4.9, an optimal channel selection was done for up to 455 channels. Figure 4.10 shows the channels always selected for each $\mathbf{R}$ matrix compared to the optimal selection of 455 channels

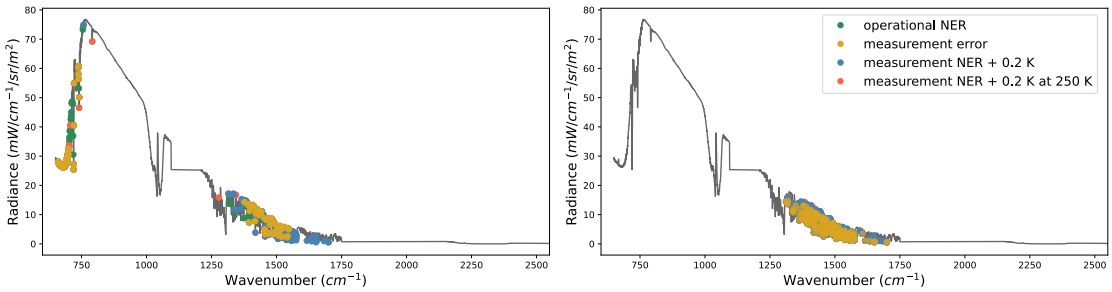

Figure 4.10 Position of the channels always selected for each **R** matrix compared to the optimal selection of 455 channels previously discussed for temperature (left) and humidity (right) superposed with a spectral radiance as a function of wavelength. The colors are the same as figure 4.9 and represent the different observation error covariance matrices.

previously discussed for temperature (left) and humidity (right). The yellow dots represent the channels that are in common for the optimal selection and the 3 other selections made with the different **R** matrices. The green, blue and red dots represent the channels that are in common between the optimal selection and the individual selections for the operational NER, the measurement error with the variable forward error and the measurement error with the constant forward error. So, for all the selections there are 163 channels always selected for temperature and 214 for humidity. Hence, there is some variability in the channel selection that can be linked to the observation error covariance matrices chosen for the experiments. However, even if the channel selections are different for various **R** matrices, the results in terms of analysis error are similar as discussed in the previous paragraph.

Also, the analysis error variance was compared between the averaged optimal se-

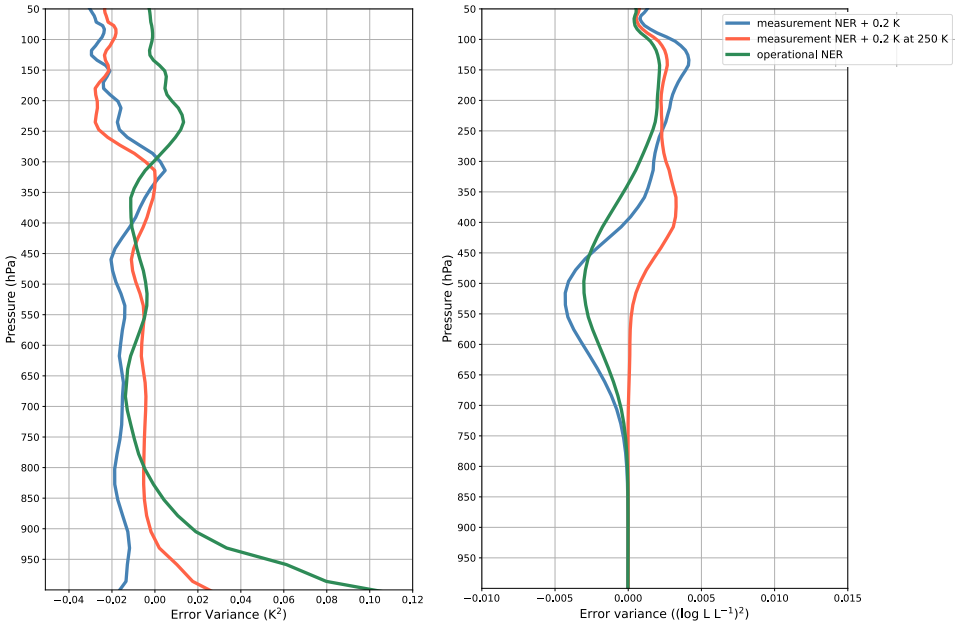

Figure 4.11 Difference in averaged analysis error between two optimal selections. The first selection is the optimal selection of 455 channels and the second is the selections calculated of 455 channels made individually for each atmospheric case averaged. It shows the difference for the operational error in green, the measurement error with the variable forward error in red and the measurement error with the constant forward error in blue.

lection of 455 channels and the selections of 455 channels made individually for each atmospheric case illustrated in figure 4.11. For temperature, both configurations with the measurement error with a forward error gives similar results between both configurations except between 300 hPa and the TOA where the optimal configuration gives better results at reducing the analysis error. There is 291 identical channels between those two configurations which can explain the similitude in the analysis error variance. For the results with the operational error, the selection made individually is better at reducing the error compared to

the averaged selection since the channel selection is tailored for the atmospheric case close to the surface and up to 850 hPa. For humidity, configurations with the operational **R** matrix and with the measurement error with a variable forward error, the optimal configuration is better at reducing the analysis error variance compared to the selections made individually between 700 hPa and 400 hPa. Also, for all configurations, between 400 hPa and the TOA, the selections made individually are better at reducing the error.

Even though the observation error covariance matrices for the variable forward error varies more than the constant forward error at 250 K and is on average larger, the results with respect to analysis error are quite similar. The difference with respect to the vertical sum for the analysis error variance is 1.4 K^2 and 0.05 $(logLL^{-1})^2$ for temperature and humidity respectively, the observation error covariance matrix with the constant forward error being slightly better. For the channels always selected for those two configurations, 291 and 334 channels are identical out of 455 which is similar to the number of channels compared to the optimal selection. Thus, it is impossible to make conclusions at this stage with respect to the use of a constant brightness temperature or of the brightness temperature of the scene.

4.5 Conclusion

The goal of this paper was to present a channel selection for the instrument CrIS on the basis of information content from the point of view of a specific system (ECCC) and to study the impact of different selections on the analysis error. Hence, channels selection were done for 50 atmospheric profiles selected in different regions for up to 400 channels of the instrument. An optimal configuration for

both temperature and humidity of 455 channels was then considered representing around 97 % of the total DFS for both temperature and humidity. In terms of analysis error, this optimal configuration reduces the error by 46.1 % and 45.6 % compared to the background error covariance for temperature and humidity respectively. This optimal configuration was then compared to two previous selections of channels done for the instrument CrIS which are from ECCC and (Carminati, 2022). The channel selection of ECCC contains 103 channels which is not enough since there is still available information that could be gained by assimilating more channels. However, compared to the selection made by (Carminati, 2022), there are 233 channels common to the two selections. The results in terms of analysis error are similar, the reduction being 44.2 % and 43.3 % for temperature and humidity respectively. The difference in the reduction of analysis error could be due to the different sets of atmospheric profiles used for the evaluations. Finally, different observation covariance matrices were considered to evaluate the impact of this matrix on channel selection. Even though the channels selected optimally were different for the various $\mathbf{R}$ matrices, the results in terms of analysis error are quite similar.

The DFS calculations used for a channel selection of an instrument depend on the background error covariance matrix $\mathbf{B}$, the observation error covariance matrix $\mathbf{R}$ and the Jacobian matrix $\mathbf{H}$ defined with respect to the atmospheric profiles chosen. It can be stated then that the same number of atmospheric profiles should be taken for each region to give the same statistical weight and also to take into consideration the variability in terms of the different atmospheric variables considered. The background error covariance matrix $\mathbf{B}$ being intrinsic to NWP centers, to study its impact on the channel selection of an instrument, an experiment could be constructed where it is the only matrix varied. Another experiment worth con-

sidering is to take the dynamic background error covariance matrix **B** instead of the static one considered in this paper. Thus, we could see the impact of those changes on the channel selection. Also, since some channel selection studies used the Desroziers method to evaluate the observation error covariance matrix, the **B** and **R** are linked. The results of this study show that there are two subsets of results in terms of analysis error. The analysis error for the operational and the **R** matrices containing a forward error gives similar results even though there is a factor of 10 between those two types of **R** matrices. On the other hand, the analysis error for the configuration with only the measurement error compared to the previous ones results in a much smaller analysis error variance which is expected since the NER is much smaller. Nevertheless, as seen with the comparison with the channel selection of (Carminati, 2022), there is only a small difference in terms of analysis error whichever selection is considered as long as there is enough channels considered. These results can help the research on channel selection with respect to the type of **R** matrices used and also bring improvement in the use of CrIS measurements for NWP systems. Further experiments will be done using **R** matrices containing interchannels covariance errors since it has been shown to improve the channel selection (Coopmann et al., 2020) and the assumption of a diagonal **R** matrix is a limitation of this paper. Also, the channels selected for CrIS could be diversified to correspond to different atmospheric conditions. An adaptive selection of channels could be considered with respect to humidity since there is a large variability in terms of this variable for channel selection. In the future, an experiment could focus on finding such an adaptive selection of channels for humidity by taking a training set of atmospheric profiles larger and that includes a sample of cases containing also extreme atmospheric situations.

CONCLUSION

Cette thèse traite de la sélection de canaux et du contenu en information pour des instruments satellitaires mesurant dans l'infrarouge. Dans la première partie, une étude théorique a été faite afin de trouver une configuration optimale d'un radiomètre mesurant dans l'infrarouge lointain optimisé pour le nombre de bandes ainsi que la largeur spectrale de celles-ci à l'aide du contenu en information. Par la suite, cette configuration optimale du radiomètre a été comparée avec un instrument satellitaire mesurant dans l'infrarouge thermique, région qui est habituellement utilisée pour profiler la température et l'humidité de l'atmosphère. Dans la deuxième partie, une sélection de canaux pour l'instrument CrIS mesurant dans l'infrarouge thermique a été calculée. Cette sélection a été comparée avec d'autres méthodes qui avaient été utilisées précédemment, soit celle provenant de ECCC et celle de Carminati (2022). De plus, plusieurs matrices de covariance d'erreur d'observations ont été considérées pour évaluer l'impact de celles-ci sur la sélection de canaux pour l'instrument CrIS.

Résumé des résultats

Une grande partie de cette thèse traite d'une méthode itérative utilisant le DFS afin de trouver une sélection de canaux optimisée pour un instrument satellitaire dans une perspective d'assimilation de données. La méthode itérative consiste à calculer le DFS pour chacune des bandes individuellement de l'instrument, de sélectionner celle ayant le plus grand DFS et de calculer le DFS de chacune de

bandes restantes une fois ajoutée à celle sélectionnée précédemment. Ce processus est fait de manière itérative pour ordonner les bandes et optimiser quelles bandes choisir. Ainsi, cette méthode fut utilisée pour deux instruments satellitaires dans cette thèse.

Le premier instrument considéré est un radiomètre mesurant dans l'infrarouge lointain. Vu que l'instrument n'est pas encore en orbite, la méthode itérative utilisant le DFS servit pour trouver une configuration optimale en termes du nombre de bandes et leurs largeurs spectrales. Ainsi trois configurations couvrant tout l'infrarouge lointain ($15\ \mu m < \lambda < 100\ \mu m$) ont été considérées, soit des bandes ayant la même largeur spectrale en terme de nombre d'onde, de longueur d'onde et d'énergie. Ainsi, la configuration optimale est 22 bandes pour la température et 7 bandes pour l'humidité. La réduction d'erreur d'analyse de cette configuration a été, par la suite, comparée à celle de l'instrument AIRS mesurant dans l'infrarouge thermique qui est assimilé dans les centres de PNT. Individuellement, le radiomètre mesurant dans l'infrarouge lointain est meilleur pour réduire l'erreur d'analyse par rapport à l'humidité entre 400 et 200 hPa. De plus, si on considère la valeur ajoutée du radiomètre mesurant dans l'infrarouge lointain après avoir assimilé AIRS, il apporte de l'information supplémentaire entre la surface et 850 hPa et entre 550 hPa et 250 hPa pour l'humidité. Il est donc possible de conclure qu'un radiomètre mesurant dans l'infrarouge lointain peut apporter des informations complémentaires aux instruments déjà existants mesurant dans l'infrarouge thermique.

Le deuxième instrument qui a été considéré est CrIS, un interféromètre à transformée de Fourier mesurant dans l'infrarouge thermique. La même méthode itérative utilisant le DFS a été utilisée pour trouver une configuration optimale en termes

du nombre de canaux à assimiler. Ainsi une configuration de 463 canaux fut trouvée. Cette configuration optimale pour CrIS a été comparée à celle de Carminati (2022) composée de 431 canaux. Les deux sélections ont 228 canaux identiques. En termes d'erreur d'analyse, pour la température, les deux configurations donnent des résultats similaires, sauf au sommet de l'atmosphère où la configuration de Carminati est meilleure pour réduire l'erreur d'analyse. Pour l'humidité, la plus grande différence entre les configurations est entre 800 et 400 hPa, ce qui est attendu, dû à la variabilité de l'humidité dans cette région de l'atmosphère. Par la suite, différentes matrices de covariance d'erreur d'observation ont été utilisées pour évaluer l'impact de cette matrice sur la sélection de canaux optimale. Même si les canaux sélectionnés de manière optimale étaient différents pour les matrices $\mathbf{R}$ considérées, les résultats en termes d'erreur d'analyse étaient similaires.

Contributions originales

La sélection de canaux d'instruments mesurant dans l'infrarouge thermique ou lointain reste un champ d'études relativement récent compte tenu que la technologie permettant ces mesures hyperspectrales a seulement une trentaine d'années. Le premier article de cette thèse constitue la première étude qui a considéré un radiomètre dans l'infrarouge lointain, car normalement un interféromètre est considéré. En utilisant un radiomètre, cela apporta une plus grande flexibilité au niveau de la sélection de canaux, car ceux-ci peuvent avoir une largeur spectrale différente et donc optimisée, tel que présenté dans le chapitre 3. De plus, selon nous, il s'agit de la première fois où l'intensité du signal et l'erreur sur la mesure sont considérées de manière séparée, ce qui permet de travailler en radiance au lieu de température de brillance. En effet, les études testant la technologie dans l'infrarouge lointain ne considèrent qu'une réduction du bruit sans considérer le

rapport signal sur bruit. Pour ce qui est de la recherche avec l'instrument CrIS, soit le chapitre 4, il n'existe aucune étude comparant différentes sélections de canaux faites par différents centres de PNT ont été comparées entre-elles.

Limitations

Comme expliqué précédemment, le contenu en information dépend de la matrice de covariance d'erreur d'observation **R**, de la matrice de covariance d'erreur de prévisions **B** ainsi que des Jacobiens. Les différentes limitations entourant cette thèse viennent des approximations qui ont été faites en lien avec ces matrices. La matrice de covariance d'erreur d'observation a été considérée comme diagonale pour l'ensemble de cette thèse. Cette approximation a été utilisée vu le contexte théorique des calculs ainsi que pour faire suite à d'autres études qui considéraient aussi une matrice de covariance d'erreur d'observation diagonale. Cependant, il a été démontré qu'utiliser une matrice qui contient des covariances dans une sélection de canaux pour un instrument dans l'infrarouge thermique diminue l'erreur d'analyse de 2 à 3 % par rapport à la température et l'humidité (Coopmann et al., 2020). Les limitations venant des Jacobiens proviennent du nombre de profils atmosphériques considérés dans les articles. Pour le premier, 6 profils ont été sélectionnés pour 8 stations en Arctique pour un total de 48 cas tandis que pour le deuxième papier, 10 stations avec 5 profils pris dans différentes régions ont été prises. Même si ce nombre de cas est similaire à plusieurs études qui ont été faites précédemment sur la sélection de canaux, un plus grand nombre de situations atmosphériques permettrait d'obtenir une configuration probablement plus robuste. De plus, les résultats présentés sont basés sur l'assimilation en une dimension afin de réduire le temps et les ressources numériques nécessaires pour la sélection itérative. Pour aller plus loin, il serait nécessaire de réaliser une ex-

périence d'assimilation de données en trois dimensions utilisant le grand volume de données actuellement assimilé dans les systèmes d'assimilations de données opérationels. Cela permettrait d'étudier l'impact de la couverture spatiale associé à différentes configurations considérées pour une future mission satellitaire ou pour l'impact d'augmenter le nombre de canaux assimilés d'un instrument.

Perspectives

Un aspect intéressant de cette thèse est l'utilisation de la méthode itérative qui permet de facilement tester différentes configurations d'un instrument autant au niveau du nombre de canaux qui devraient être assimilés que pour trouver une configuration optimale en termes de largeur spectrale et du nombre de bandes dépendant des variables étudiées. De plus, cette méthode itérative utilisant le DFS permet de trouver un nombre optimal de canaux qui devraient être assimilés pour les centres de PNT et de trouver une sélection de canaux meilleure qu'avec la méthode des Jacobiens.

BIBLIOGRAPHIE

Andersson, E., Hollingsworth, A., Kelly, G., Lönnberg, P., Pailleux, J. & Zhang, Z. (1991). Global observing system experiments on operational statistical retrievals of satellite sounding data. *Monthly weather review*, *119*(8), 1851–1865.

Aumann, H. H., Chahine, M. T., Gautier, C., Goldberg, M. D., Kalnay, E., McMillin, L. M., Revercomb, H., Rosenkranz, P. W., Smith, W. L., Staelin, D. H. et al. (2003). Airs/amsu/hsb on the aqua mission: Design, science objectives, data products, and processing systems. *IEEE Transactions on Geoscience and Remote Sensing*, *41*(2), 253–264.

Bantges, R., Brindley, H., Chen, X., Huang, X., Harries, J. & Murray, J. (2016). On the detection of robust multidecadal changes in earth's outgoing longwave radiation spectrum. *Journal of Climate*, *29*(13), 4939–4947.

Berk, A., Anderson, G. P., Acharya, P. K., Bernstein, L. S., Muratov, L., Lee, J., Fox, M., Adler-Golden, S. M., Chetwynd, J. H., Hoke, M. L. et al. (2005). Modtran 5: a reformulated atmospheric band model with auxiliary species and practical multiple scattering options: update. In *Proc. of SPIE Vol*, volume 5806, pp. 663.

Bloom, H. (2001). The cross-track infrared sounder (cris): A sensor for operational meterological remote sensing. In *Fourier Transform Spectroscopy*, pp. JTuB1. Optical Society of America.

Blumstein, D., Chalon, G., Carlier, T., Buil, C., Hebert, P., Maciaszek, T., Ponce, G., Phulpin, T., Tournier, B., Simeoni, D. et al. (2004). Iasi instrument: Technical overview and measured performances. In *Proc. of SPIE Vol*, volume 5543, pp. 197.

Bormann, N., Collard, A. & Bauer, P. (2010). Estimates of spatial and interchannel observation-error characteristics for current sounder radiances for numerical weather prediction. ii: Application to airs and iasi data. *Quarterly Journal of the Royal Meteorological Society*, *136*(649), 1051–1063.

Boullot, N., Rabier, F., Langland, R., Gelaro, R., Cardinali, C., Guidard, V., Bauer, P. & Doerenbecher, A. (2016). Observation impact over the southern

polar area during the concordiasi field campaign. *Quarterly Journal of the Royal Meteorological Society*, *142*(695), 597–610.

Buehner, M., McTaggart-Cowan, R., Beaulne, A., Charette, C., Garand, L., Heilliette, S., Lapalme, E., Laroche, S., Macpherson, S. R., Morneau, J. et al. (2015). Implementation of deterministic weather forecasting systems based on ensemble–variational data assimilation at environment canada. part i: The global system. *Monthly Weather Review*, *143*(7), 2532–2559.

Canas, T. A., Murray, J. & Harries, J. E. (1997). Tropospheric airborne fourier transform spectrometer (tafts). In *Satellite remote sensing of clouds and the atmosphere II*, volume 3220, pp. 91–102.

Carli, B., Barbis, A., Harries, J. E. & Palchetti, L. (1999). Design of an efficient broadband far-infrared fourier-transform spectrometer. *Applied optics*, *38*(18), 3945–3950.

Carminati, F. (2022). A channel selection for the assimilation of cris and hiras instruments at full spectral resolution. *Quarterly Journal of the Royal Meteorological Society*, *148*(744), 1092–1112.

Chang, K.-W., L'Ecuyer, T. S., Kahn, B. H. & Natraj, V. (2017). Information content of visible and midinfrared radiances for retrieving tropical ice cloud properties. *Journal of Geophysical Research: Atmospheres*, *122*(9), 4944–4966.

Clerbaux, C., Boynard, A., Clarisse, L., George, M., Hadji-Lazaro, J., Herbin, H., Hurtmans, D., Pommier, M., Razavi, A., Turquety, S. et al. (2009). Monitoring of atmospheric composition using the thermal infrared iasi/metop sounder. *Atmospheric Chemistry and Physics*, *9*(16), 6041–6054.

Clough, S. A., Iacono, M. J. & Moncet, J.-L. (1992). Line-by-line calculations of atmospheric fluxes and cooling rates: Application to water vapor. *Journal of Geophysical Research: Atmospheres*, *97*(D14), 15761–15785.

Collard, A. (2007). Selection of iasi channels for use in numerical weather prediction. *Quarterly Journal of the Royal Meteorological Society: A journal of the atmospheric sciences, applied meteorology and physical oceanography*, *133*(629), 1977–1991.

Collard, A. & McNally, A. (2009). The assimilation of infrared atmospheric sounding interferometer radiances at ecmwf. *Quarterly Journal of the Royal Meteorological Society*, *135*(641), 1044–1058.

Coopmann, O., Fourrié, N. & Guidard, V. (2022). Analysis of mtg-irs observations and general channel selection for numerical weather prediction

models. *Quarterly Journal of the Royal Meteorological Society*, *148*(745), 1864–1885.

Coopmann, O., Guidard, V., Fourrié, N., Josse, B. & Marécal, V. (2020). Update of infrared atmospheric sounding interferometer (iasi) channel selection with correlated observation errors for numerical weather prediction (nwp). *Atmospheric Measurement Techniques*, *13*(5), 2659–2680.

Coursol, L., Libois, Q., Gauthier, P. & Blanchet, J.-P. (2020). Optimal configuration of a far-infrared radiometer to study the arctic winter atmosphere. *Journal of Geophysical Research: Atmospheres*, *125*(14), e2019JD031773.

Crevoisier, C., Clerbaux, C., Guidard, V., Phulpin, T., Armante, R., Barret, B., Camy-Peyret, C., Chaboureau, J.-P., Coheur, P.-F., Crépeau, L. et al. (2014). Towards iasi-new generation (iasi-ng): impact of improved spectral resolution and radiometric noise on the retrieval of thermodynamic, chemistry and climate variables. *Atmospheric Measurement Techniques*, *7*(12), 4367–4385.

Desroziers, G., Berre, L., Chapnik, B. & Poli, P. (2005). Diagnosis of observation, background and analysis-error statistics in observation space. *Quarterly Journal of the Royal Meteorological Society: A journal of the atmospheric sciences, applied meteorology and physical oceanography*, *131*(613), 3385–3396.

Divakarla, M. G., Barnet, C. D., Goldberg, M. D., McMillin, L. M., Maddy, E., Wolf, W., Zhou, L. & Liu, X. (2006). Validation of atmospheric infrared sounder temperature and water vapor retrievals with matched radiosonde measurements and forecasts. *Journal of Geophysical Research: Atmospheres*, *111*(D9).

Durre, I., Reale, T., Carlson, D., Christy, J., Uddstrom, M., Gelman, M., Thorne, P. & contributions from 23 additional Workshop participants (2005). Improving the usefulness of operational radiosonde data. *Bulletin of the American Meteorological Society*, *86*(3), 411–418.

Durre, I., Vose, R. S. & Wuertz, D. B. (2006). Overview of the integrated global radiosonde archive. *Journal of Climate*, *19*(1), 53–68.

Eyre, J., Kelly, G., McNally, A., Andersson, E. & Persson, A. (1993). Assimilation of tovs radiance information through one-dimensional variational analysis. *Quarterly Journal of the Royal Meteorological Society*, *119*(514), 1427–1463.

Flanner, M., Huang, X., Chen, X. & Krinner, G. (2018). Climate response to negative greenhouse gas radiative forcing in polar winter. *Geophysical Research Letters*, *45*(4), 1997–2004.

Fourrié, N. & Thépaut, J.-n. (2003). Evaluation of the airs near-real-time channel selection for application to numerical weather prediction. *Quarterly Journal of the Royal Meteorological Society*, *129*(592), 2425–2439.

Gambacorta, A. & Barnet, C. D. (2012). Methodology and information content of the noaa nesdis operational channel selection for the cross-track infrared sounder (cris). *IEEE transactions on geoscience and remote sensing*, *51*(6), 3207–3216.

Garand, L., Heilliette, S. & Buehner, M. (2007). Interchannel error correlation associated with airs radiance observations: Inference and impact in data assimilation. *Journal of applied meteorology and climatology*, *46*(6), 714–725.

Garand, L., Turner, D., Larocque, M., Bates, J., Boukabara, S., Brunel, P., Chevallier, F., Deblonde, G., Engelen, R., Hollingshead, M. et al. (2001). Radiance and jacobian intercomparison of radiative transfer models applied to hirs and amsu channels. *Journal of Geophysical Research: Atmospheres*, *106*(D20), 24017–24031.

Han, Y., Revercomb, H., Cromp, M., Gu, D., Johnson, D., Mooney, D., Scott, D., Strow, L., Bingham, G., Borg, L. et al. (2013). Suomi npp cris measurements, sensor data record algorithm, calibration and validation activities, and record data quality. *Journal of Geophysical Research: Atmospheres*, *118*(22), 12–734.

Harries, J., Carli, B., Rizzi, R., Serio, C., Mlynczak, M., Palchetti, L., Maestri, T., Brindley, H. & Masiello, G. (2008). The far-infrared earth. *Reviews of Geophysics*, *46*(4).

Joiner, J., Brin, E., Treadon, R., Derber, J., Van Delst, P., Da Silva, A., Le Marshall, J., Poli, P., Atlas, R., Bungato, D. et al. (2007). Effects of data selection and error specification on the assimilation of airs data. *Quarterly Journal of the Royal Meteorological Society: A journal of the atmospheric sciences, applied meteorology and physical oceanography*, *133*(622), 181–196.

Kaplan, L. D., Chahine, M. T., Susskind, J. & Searl, J. E. (1977). Spectral band passes for a high precision satellite sounder. *Applied optics*, *16*(2), 322–325.

L'Ecuyer, T. (2019). The polar radiant energy in the far infrared experiment (prefire): A far infrared mission to improve estimates of the polar energy

budgets. In *Geophysical research abstracts*, volume 21.

Lewis, J. M., Lakshmivarahan, S. & Dhall, S. (2006). *Dynamic data assimilation: a least squares approach*, volume 13. Cambridge University Press.

Libois, Q. & Blanchet, J.-P. (2017). Added value of far-infrared radiometry for remote sensing of ice clouds. *Journal of Geophysical Research: Atmospheres*.

Libois, Q., Ivanescu, L., Blanchet, J.-P., Schulz, H., Bozem, H., Leaitch, W. R., Burkart, J., Abbatt, J. P., Herber, A. B., Aliabadi, A. A. et al. (2016a). Airborne observations of far-infrared upwelling radiance in the arctic. *Atmospheric Chemistry and Physics*, *16*(24), 15689–15707.

Libois, Q., Proulx, C., Ivanescu, L., Coursol, L., Pelletier, L. S., Bouzid, Y., Barbero, F., Girard, É. & Blanchet, J.-P. (2016b). A microbolometer based far infrared radiometer to study thin ice clouds in the arctic. *Atmospheric Measurement Techniques*, *9*(4), 1817.

Lupu, C., Gauthier, P. & Laroche, S. (2011). Evaluation of the impact of observations on analyses in 3d-and 4d-var based on information content. *Monthly Weather Review*, *139*(3), 726–737.

McNally, A., Watts, P., A Smith, J., Engelen, R., Kelly, G., Thépaut, J. & Matricardi, M. (2006). The assimilation of airs radiance data at ecmwf. *Quarterly Journal of the Royal Meteorological Society*, *132*(616), 935–957.

Merrelli, A. & Turner, D. D. (2012). Comparing information content of upwelling far-infrared and midinfrared radiance spectra for clear atmosphere profiling. *Journal of Atmospheric and Oceanic Technology*, *29*(4), 510–526.

Mertens, C. J. (2002). Feasibility of retrieving upper tropospheric water vapor from observations of far-infrared radiation. In *Optical Spectroscopic Techniques, Remote Sensing, and Instrumentation for Atmospheric and Space Research IV*, volume 4485, pp. 191–201. International Society for Optics and Photonics.

Mlynczak, M., Johnson, D. G. & Kratz, D. P. (2007). The far-infrared spectrum: Exploring a new frontier in the remote sensing of the earth's climate. In *Hyperspectral Imaging and Sounding of the Environment*, pp. HMA1. Optical Society of America.

Mlynczak, M. G., Harries, J. E., Rizzi, R., Stackhouse, P. W., Kratz, D. P., Johnson, D. G., Mertens, C. J., Garcia, R. R. & Soden, B. J. (2002).

Far-infrared: a frontier in remote sensing of earth's climate and energy balance. In *International Symposium on Optical Science and Technology*, pp. 150–158. International Society for Optics and Photonics.

Mlynczak, M. G., Johnson, D. G., Bingham, G., Jucks, K., Traub, W., Gordley, L. & Harries, J. (2004). The far-infrared spectroscopy of the troposphere(first) project. In *Proc. SPIE*, volume 5659, pp. 81–87.

Mlynczak, M. G., Johnson, D. G., Latvakoski, H., Jucks, K., Watson, M., Kratz, D. P., Bingham, G., Traub, W. A., Wellard, S. J., Hyde, C. R. et al. (2006). First light from the far-infrared spectroscopy of the troposphere (first) instrument. *Geophysical research letters*, *33*(7).

Müller, R., Kunz, A., Hurst, D. F., Rolf, C., Krämer, M. & Riese, M. (2016). The need for accurate long-term measurements of water vapor in the upper troposphere and lower stratosphere with global coverage. *Earth's Future*, *4*(2), 25–32.

Noh, Y.-C., Sohn, B.-J., Kim, Y., Joo, S., Bell, W. & Saunders, R. (2017). A new infrared atmospheric sounding interferometer channel selection and assessment of its impact on met office nwp forecasts. *Advances in Atmospheric Sciences*, *34*, 1265–1281.

Palchetti, L., Olivieri, M., Pompei, C., Labate, D., Brindley, H., Di Natale, G. & Bianchini, G. (2016). The far infrared fts for the forum mission. In *Fourier Transform Spectroscopy*, pp. FTu3C–1. Optical Society of America.

Proulx, C., Williamson, F., Allard, M., Baldenberger, G., Gay, D., Garcia-Blanco, S., Côté, P., Martin, L., Larouche, C., Ilias, S. et al. (2009). The earthcare broadband radiometer detectors. In *Proc. SPIE*, volume 7453, pp. 74530S.

Prunet, P., Thépaut, J.-N. & Cassé, V. (1998). The information content of clear sky iasi radiances and their potential for numerical weather prediction. *Quarterly Journal of the Royal Meteorological Society*, *124*(545), 211–241.

Purser, R. & Huang, H. (1993). Estimating effective data density in a satellite retrieval or an objective analysis. *Journal of applied meteorology*, *32*(6), 1092–1107.

Rabier, F., Fourrié, N., Chafäi, D. & Prunet, P. (2002). Channel selection methods for infrared atmospheric sounding interferometer radiances. *Quarterly Journal of the Royal Meteorological Society*, *128*(581), 1011–1027.

Rizzi, R., Serio, C. & Amorati, R. (2002). Sensitivity of broadband and

spectral measurements of outgoing radiance to changes in water vapor content. In *Optical Spectroscopic Techniques, Remote Sensing, and Instrumentation for Atmospheric and Space Research IV*, volume 4485, pp. 181–190.

Rodgers, C. D. (1998). Information content and optimisation of high spectral resolution remote measurements. *Advances in Space Research*, *21*(3), 361–367.

Rodgers, C. D. (2000). *Inverse methods for atmospheric sounding: theory and practice*, volume 2. World scientific.

S Pelletier, L., Libois, Q., Laurence, C. & Blanchet, J.-P. (2017). Winter far infrared measurements in the high arctic. *AGUFM*, *2017*, A41A–2245.

Saunders, R., Hocking, J., Turner, E., Rayer, P., Rundle, D., Brunel, P., Vidot, J., Roquet, P., Matricardi, M., Geer, A. et al. (2018). An update on the rttov fast radiative transfer model (currently at version 12). *Geoscientific Model Development*, *11*(7).

Serreze, M. C., Barrett, A. P. & Stroeve, J. (2012). Recent changes in tropospheric water vapor over the arctic as assessed from radiosondes and atmospheric reanalyses. *Journal of Geophysical Research: Atmospheres*, *117*(D10).

Shahabadi, M. B. & Huang, Y. (2014). Measuring stratospheric h2o with an airborne spectrometer. *Journal of Atmospheric and Oceanic Technology*, *31*(7), 1502–1515.

Shahabadi, M. B., Huang, Y. & Moreau, L. M. (2015). Measuring stratospheric h 2 o with an airborne spectrometer: Simulation with realistic detector characteristics. *IEEE Journal of Selected Topics in Applied Earth Observations and Remote Sensing*, *8*(7), 3541–3545.

Sherwood, S., Roca, R., Weckwerth, T. & Andronova, N. (2010). Tropospheric water vapor, convection, and climate. *Reviews of Geophysics*, *48*(2).

Smith, A., Atkinson, N., Bell, W. & Doherty, A. (2015). An initial assessment of observations from the suomi-npp satellite: data from the cross-track infrared sounder (cris). *Atmospheric Science Letters*, *16*(3), 260–266.

Smith, W. (1979). Teh tiros-n operational vertical sounder. *Bull. Am. Meteorol. Soc.*, *60*, 1177–1187.

Susskind, J., Barnet, C. D. & Blaisdell, J. M. (2003). Retrieval of atmospheric and surface parameters from airs/amsu/hsb data in the presence of clouds.

IEEE Transactions on Geoscience and Remote Sensing, *41*(2), 390–409.

Vittorioso, F., Guidard, V. & Fourrié, N. (2021). An infrared atmospheric sounding interferometer–new generation (iasi-ng) channel selection for numerical weather prediction. *Quarterly Journal of the Royal Meteorological Society*, *147*(739), 3297–3317.

Wark, D. & Hilleary, D. (1969). Atmospheric temperature: Successful test of remote probing. *Science*, *165*(3899), 1256–1258.

Wielicki, B. A., Young, D., Mlynczak, M., Thome, K., Leroy, S., Corliss, J., Anderson, J., Ao, C., Bantges, R., Best, F. et al. (2013). Achieving climate change absolute accuracy in orbit. *Bulletin of the American Meteorological Society*, *94*(10), 1519–1539.

Xiong, X., Wenny, B. N., Wu, A., Barnes, W. L. & Salomonson, V. V. (2008). Aqua modis thermal emissive band on-orbit calibration, characterization, and performance. *IEEE Transactions on Geoscience and Remote Sensing*, *47*(3), 803–814.